# Examining Passive Flow Control using High Speed Shadowgraph Images in a Mach 1.5 Cavity Flow Field

**Ryan F. Schmit[1], James E. Grove[1] and Anwar Ahmed[2]**
U.S Air Force Research Laboratory, [1]2130 Eight Street Wright-Patterson Air Force Base, OH 45433, USA. ryan.schmit@us.af.mil, james.grove@us.af.mil
Auburn University, [2]211 Aerospace Engineering Bldg. Auburn, AL 36849-5338 USA
aahmed@eng.auburn.edu

Received date 10/5/2013; Accepted date 18/11/2013

**ABSTRACT**

A rectangular cavity with an L/D of 5.67 was tested at Mach 1.5 with a corresponding Reynolds number of $7.35 \times 10^6$/m. High speed shadowgraph movies were simultaneously sampled with dynamic pressure sensors at 75 kHz. Fourier analysis was performed on the high speed movies as well as the dynamic pressure data, which resulted in the determination of spatial and temporal characteristics of the dominant cavity frequencies in the flow field. Four passive flow control devices were tested, two of which have historically performed well at reducing the acoustic tones and broadband noise levels. The other two devices were less effective. Flow physics based on the detailed analysis of the high speed shadowgraphs and dynamic pressures sensors is presented.

## 1. INTRODUCTION

For over 60 years, weapon bays, landing gear, and other similar cavities has been examined by numerous researchers throughout the world. Starting from the pioneering work of Krishnamurty [1], Roshko [2], Rossiter [3] and others, the researchers have employed a variety of analytical and experimental techniques to examine and understand the physics that occurs inside the cavity for various Length-to-Depth ratios and for a combination of Mach and Reynolds numbers. Heller and Bliss [4], Tam and Block [5] as well as Bauer and Dix [6] have attempted to improve the physical understand of the cavity through their works respectively.

Since Rossiter [3], reducing the cavity tone and the broadband noise through the use of geometry modification and flow control has become an important objective of cavity research. A review paper by Cattafesta et al. [7] outlines work of numerous researchers who have examined the effects of geometric modification, active flow control and feedback flow control techniques applied to cavity flows. All have shown some success at reducing either cavity tones, the broad band noise or both, however, most techniques have remained limited in scope due to their sensitivity to a number of flow variables including the state of the boundary layer prior to separation [8].

There are two types of wind tunnel cavity models that have been tested over the years, in-floor cavity models and sting based generic aircraft weapons bay cavity models. In-floor cavity models like Moon et al. [9], Murray and Elliot [10], and Dudley and Ukeiley [11] are smaller sized cavity models that are simply a cut-out from one of the side wall of a wind tunnel. Typically these cavities span the entire width of the tunnel for non-intrusive optical access, e.g. Particle Image Velocimetry (PIV), Doppler Anemometry (LDA) and Planar Induced Florescence (PLIF) and in turn also result in higher width to depth (W/D) ratios as compared to generic aircraft weapons bay cavity models. In-floor cavity models however are easy to work with as the control methodology can easily be implemented compared to their sting mounted counterparts.

The first sting based generic aircraft weapons bay cavity model developed by Kaufman and Clark [12] was the Turbulence Reduction Cavity (TRC) model and was tested several times from the mid 1970's to

the late 1980's. These tests provided acoustic measurements and oil flow visualization inside the cavity as well as schlieren photographs of the flow field outside of the cavity for the numerous passive flow control devices. Several other sting mounted generic cavity models have been tested in various wind tunnels in the past two decades are: the Weapons Internal Carriage and Separation (WICS) cavity model [6], the Defence Evaluation and Research Agency (DERA) cavity model [13] and the High-Frequency Excitation Active Flow Control for Supersonic Weapons Release (HIFEX) cavity model [14]. The three sting based cavity models utilized in some form, passive and open loop flow control devices that resulted in the reduction of the acoustic tones and the overall sound pressure levels, however the effect of the flow control devices on the flow field remained unknown. With the subsequent development of state of the art non-intrusive flow field measuring techniques, such as PIV, LDA and PLIF, new possibilities arose however the original TRC model could not provide the necessary optical access and therefore a new Optical Turbulence Reduction Cavity (OTRC) was build [15]. The OTRC was designed with non-intrusive flow field measurements in mind, not only to acquire an improved understanding of the underlining flow physics surround a rectangular cavity, but also an improved understanding how different flow control devices fundamentally change the flow field around the cavity for the better or worse.

Schmit et al. [16] examined the cavity flow physics using the ORTC cavity model and experimental techniques employed previously. The objective of the present work was to reexamine the fundamental differences between the cavity flow physics using four different geometric modifications that have been used on prior experimental and computational investigations but have had temporal and/or visualization limitations. By understanding the subtle differences in the flow physics between the geometry modifications, new actuators and control methodologies can be developed to take advantage of the new insights from flow physics in reducing the cavity tones as well as the broadband noise to levels suitable for future aircraft weapons bays.

## 2. EXPERIMENTAL SETUP

### 2.1. Trisonic Gasdynamics Facility

The Trisonic Gasdynamics Facility (TGF) shown in Figure 1 is located on Area B of Wright-Patterson Air Force Base. The tunnel was built in the 1950's to provide researchers a wind tunnel to study complex flow configurations in the subsonic and supersonic regimes within the Air Force and DoD organizations. When coupled and synchronized, the 2610 kW and 3729 kW motors provide the power to the wind tunnel to achieve subsonic velocities from Mach 0.23 to 0.87, and discrete supersonic Mach numbers of 1.5, 1.9, 2.3 and 3.0 with interchangeable nozzle blocks. The test section total pressure is adjustable from 51 to 202 kPa. The maximum subsonic Reynolds number for the tunnel is 8.2 million per meter and the maximum subsonic dynamic pressure is 16.76 kPa. The maximum supersonic Reynolds number is 16.4 million per meter and the maximum supersonic dynamic pressure is 47.9 kPa. The stagnation temperature is held constant at 297°K.

The test section is 0.61 meter high, 0.61 meter wide and 1.219 meter long with two optically flat 0.66 meter diameter viewing windows on either side of the test section. The primary model support is a crescent mounted sting, which can be used to reach various attitudes, or model orientations, including pitch from –1° to + 18.5°, roll from –90° to + 180° [17].

### 2.2. Optical Turbulence Reduction Cavity (OTRC) Model

Figure 2 shows the mounted OTRC model and the coordinate system. The cavity dimensions are: length 21.6 cm, depth 3.8 cm and width 6.4 cm, the L/D is 5.67 and is approximately 1/20$^{th}$ full scale.

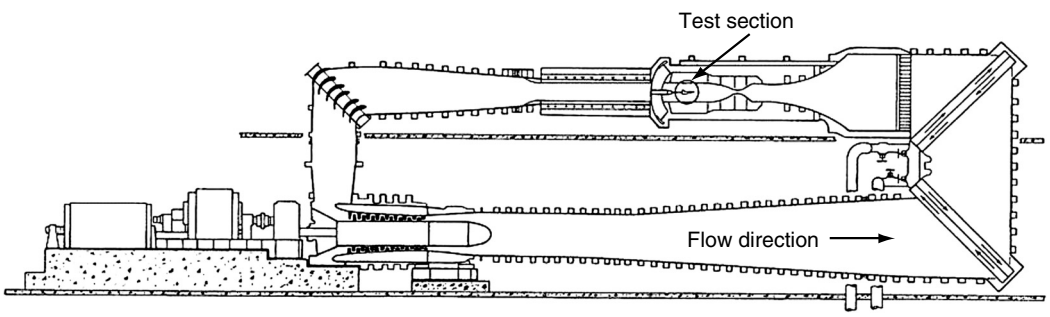


Figure 1. Trisonic gasdynamics facility.

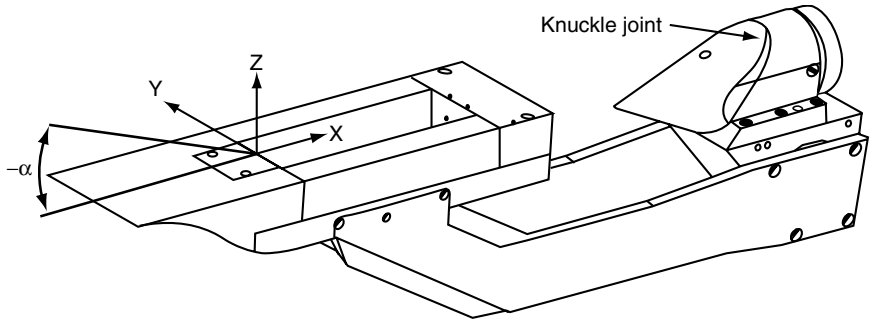


Figure 2. Isometric sketch of the optical turbulence reduction cavity model.

The fore-body of the model is 17.9 cm long and is 12.7 cm wide.

The forward and aft wall blocks of the cavity are designed to incorporate a variety of flow control devices without compromising overall geometry of the cavity. Tests were conducted at a Mach number of 1.5, total pressure of 51.9 kPa, total temperature of 301°K, air density of 0.232 kg/m$^3$ and Reynolds Number per meter of 7.35x10$^6$.

To ensure an attached boundary layer along the fore body the cavity, the pitch angle, $\alpha$, was set to +3/4°. There are two methods to set the pitch angle for this model, at the tunnel support crescent and/or at the sting knuckle joint. The knuckle joint, shown in Figure 2, is needed because the crescent does not have yaw capability when the model is rolled 90°. When the cavity roll angle is 0°, i.e. the cavity ceiling is normal to the schlieren optical axis, the crescent is adjusted to set the pitch angle to +3/4°, while the knuckle joint is set to 0°. When the cavity is rolled 90°, i.e. the cavity ceiling is normal to the tunnel windows, the crescent angle is set to 0° while the knuckle joint sets the pitch angle to +3/4°.

Since the cavity model was built for the application of non-intrusive diagnostic techniques there are three interchangeable optical quality fused silica windows available for this model. The two side walls windows are replaceable with two aluminum blanks if required. The ceiling window is also interchangeable with an aluminum blank. Figure 3a shows a sketch of the sensors located in the cavity ceiling: two thermocouples (T1 and T2), 3 static pressure ports (P1, P2 and P3) and up to 7 dynamic pressure sensors (End 1thru End 7). For this test, 6 of the 7 dynamic pressure sensors were properly

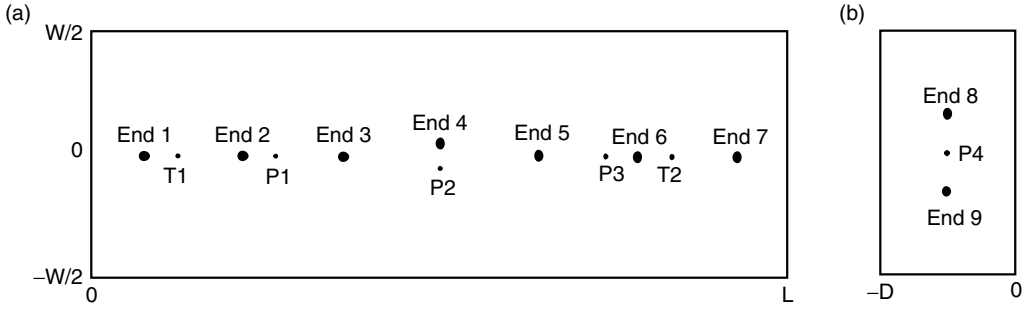


Figure 3. Sensor locations inside the cavity (a) cavity ceiling, (b) aft wall.

Table 1. Locations of dynamic pressure sensors

| Sensor | x/L | y/2W | z/D |
|---|---|---|---|
| End 1 | 0.05 | 0.00 | –1.00 |
| End 2 | 0.20 | 0.00 | –1.00 |
| End 3 | 0.35 | 0.00 | –1.00 |
| End 5 | 0.65 | 0.00 | –1.00 |
| End 6 | 0.80 | 0.00 | –1.00 |
| End 7 | 0.95 | 0.00 | –1.00 |
| End 8 | 1.00 | 0.32 | –0.50 |
| End 9 | 1.00 | –0.32 | –0.50 |

working and their locations inside the cavity are given in Table 1. Figure 3b shows the sketch of sensors located in the cavity's aft wall: two dynamic pressure sensors (End 8 and End 9) and one static pressure (P4). The aft wall dynamic pressure sensors locations are also listed in Table 1.

### 2.3. Passive Flow Control Devices

In applying control methodologies to cavity flows, both the state of the approaching boundary layer prior to separation, and the separated turbulent shear layer play an important role in cavity acoustics. It has been shown that the streamwise scales of turbulence decrease significantly in the supersonic turbulent boundary layer [18], and likewise the compressibility tends to reduce the spread of shear layer [19,20] resulting in a reduction in the Reynolds stresses and entrainment [21]. However the wavelength and intensity of the acoustic waves are much larger than the turbulence scales [22].

For an inviscid shear layer the results of Blumen et. al [23] show that compressibility also prevents the growth of Kelvin-Helmholtz modes and their interactions. For flow control applications, it is therefore important to introduce known disturbances of relatively high amplitude to offset the dampening of the secondary structures in the post-separated shear layer. Consequently the edge tones thus produced by the shear layer impinging on the rear corner of the cavity retains energy in the lower wave number range. Experiments by Papamoschou and Roshko [24] have clearly shown that the spread rate of the turbulent shear layer largely depended on the Mach number and is independent of the transverse density gradients.

Recently Schulin and Trofimov [25] reported that the vorticity generated by supercritical elements such as dots and triangular prisms placed in a supersonic turbulent boundary layer survived up to $10^4$ times the height of the generators, and the disturbances amplified in the presence of an adverse pressure gradient. This shows the effectiveness of passive flow control techniques.

The passive flow control devices are broadly categorized as those applied to the leading edge, and the trailing edge of a cavity. Leading edge devices include spoilers, wedges, cylinders, etc. and are primarily intended for the thickening of the separated shear layer [15]. The trailing edge treatment on the other hand is designed to deflect the shear layer and or acoustic wave by shaping of the rear wall [26].

For the present experiments, the passive devices consisted of the flat spoiler, large 3D backward facing steps, ridges and 6 mm rod at the leading edge. The rationale behind the entire set of passive control device will be explained below.

One of the oldest known and used geometry modifying control devices is the flat spoiler that spans

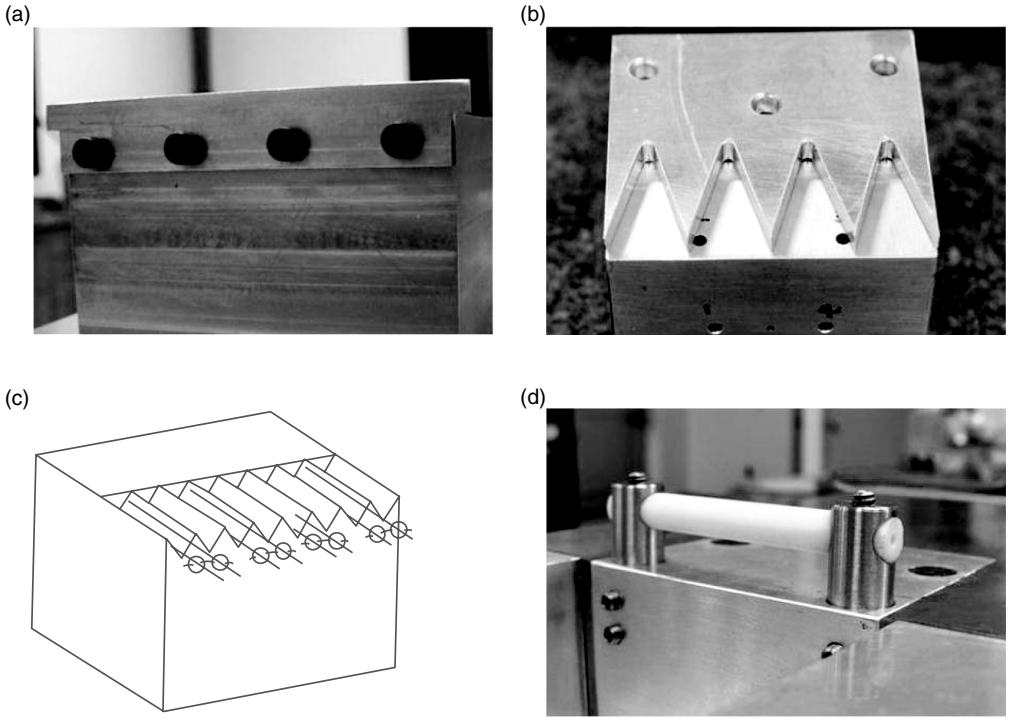


Figure 4. Details of the passive flow control devices, (a) Flat Spoiler, (b) Large 3D backward facing steps, (c) Ridges, (d) 6 mm Rod.

width of the cavity and is shown in Figure 4a. The flat spoiler is 63.5 mm wide, protrudes 4.06 mm above the cavity waterline and is 1.6 mm thick. One possible explanation as to why the flat spoiler works is that it lifts the boundary layer over the cavity, reducing the shear layers ability to hit the rear wall corner and penetrate the cavity [27].

The next two devices tested use a similar approach. When the boundary layer separates at the edge of a back step, the vorticity in the separated boundary layer rolls up and forms streamwise vortices at the base of the V-groove. Since the vortices in the base of the V-groove are very stable [28], they introduce streamwise vorticity in the shear layer resulting in thickening of the shear layer due to entrainment and introduce oblique disturbances as they are more stable [29]. Figure 4b shows the large 3D backward facing steps. The four V-shaped cuts are 63.5 mm wide and extend 2.54 mm upstream and are 4 mm deep. This device is used to introduce streamwise vortical structures in the shear layer.

Figure 4c shows another V-shaped device with streamwise grooves of 60 degrees interior angle with depth on the same order of the boundary layer displacement thickness. Streamwise vortex pairs are depicted in Figure 4c. In this paper this device is referred to as Ridges.

The last passive control device is the rod in a cross flow, and is shown in Figure 4d. The 6 mm diameter ceramic rod is 63.5 mm wide and the gap between the rod and the cavity waterline is 2.54 mm. The rod is held in position using two 8 mm diameter vertical posts. The gap between the rod and the cavity waterline is adjustable using set screws. Stanek [26] describes the development and theory Accordingly, the vortex shedding from rod interferes with the vorticity in the shear layer and prevents the growth of normal modes. The rod diameter is 2/3 the height of the boundary layer thickness and effective gap is 1 rod diameter.

### 2.5. Shadowgraph Setup

Shadowgraph photography is one of the oldest non-intrusive flow diagnostic techniques available in the TGF. For more information about this technique please refer to Settles [30]. Figure 5 shows a sketch of a standard Z-type shadowgraph setup with a 350 Watt arc lamp that is used as the light source. The light reflects off a parabolic mirror, passes through the TGF test section, then through the control room window, where it finally reflects off the second parabolic mirror. Once the light arrives onto the optical table it encounters a 50/50 plate beam splitter that is set at approximately 45° to the light's path. The reflected light from the plate beam splitter is used for data acquisition. The light that passes through the plate beam splitter is used to monitor tunnel condition using a 30 Hz astronomy camera with a 35mm lens. The tunnel and model windows were cleaned as needed.

A Photron FASTCAM SA1 with an AF Zoom-NIKKOR 80-200 mm f/2.8D ED lens was used to capture the shadowgraph images. Because of the amount of light lost by a knife edge, the FASTCAM

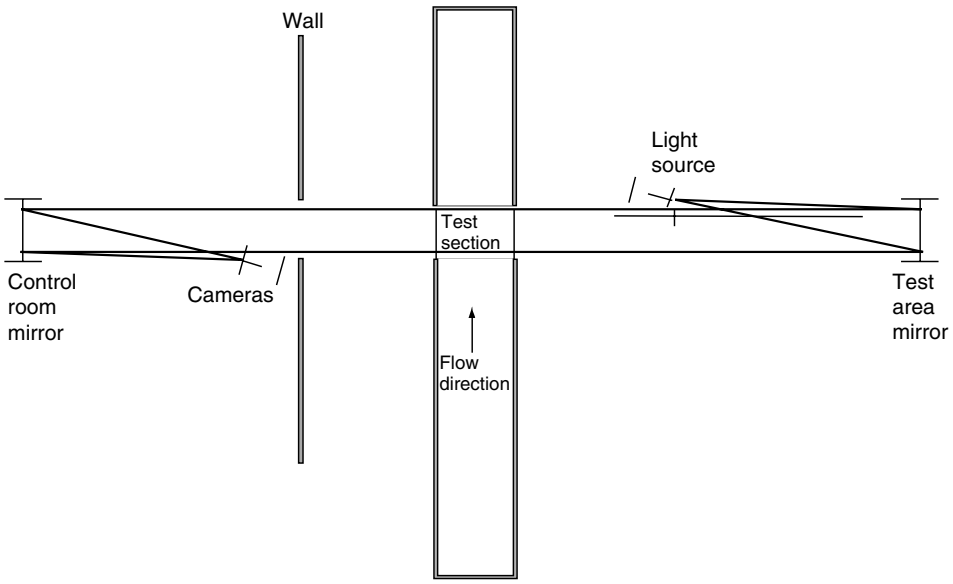


Figure 5. Sketch of TGF's shadowgraph setup.

was setup for shadowgraph imaging. The camera's frame rate was set to 75000 Hz which provided a maximum resolution of 512 pixels horizontally by 128 pixels vertically. The electronic shutter speed was 1/2,700,000 sec., or 0.37 $\mu$sec. The pixel depth for this camera is $2^8$ with three channels of color, RGB.

### 2.6. Data Acquisition and Analysis

The thermocouple data was acquired using Omega 5TC-TT-J24-72 sensors, which have a range from 73° K to 623° K and were sampled at 1 kHz, averaged, and recorded at 5 Hz using a National Instruments Data Acquisition card. The static pressure data was acquired with a Pressure Systems Model 8400 Scanner with a 0 to 103 kPa differential module and was sampled at 100 Hz, averaged, and also recorded at 5 Hz. Both the temperature and static pressure sensors were check-calibrated in the model and have an uncertainty of 0.1% Full Scale (FS). The dynamic pressure data was acquired using Endevco Model 8507C-2 pressure transducers, with a pressure range of 0 to 13.8 kPa gauge and an uncertainty of 0.2% FS. The dynamic pressure sensors were also check-calibrated in the model and have an error uncertainty of 1.0% FS. Since this model has been installed several times over the past few years the repeatability of the results has remained within ±1 dB.

The dynamic data was acquired on the RQVX high-speed data (Whisper) system. This system performs simultaneous sample-and-hold acquisition at a rate of 75 kHz for data records 2 seconds in length. Digital images were simultaneously acquired during several dynamic pressure acquisition cycles. To accomplish image acquisition, a 5 V TTL trigger signal was sent from the high speed data acquisition system to the FASTCAM digital camera. Tn entire segment of seconds of high speed video was kept for a handful of test points, because of the large size of .avi file (27.4 GB). For all other test points the first 5000 images were retained because of under 1GB file size. For the dynamic pressure data, 150,000 samples were collected for each channel.

A Discrete Fourier Transform (DFT) was used to convert the blocks of dynamic pressure and shadowgraph video data into the frequency domain. Prior to the DFT of the shadowgraph video, each pixel was converted from RGB to grayscale using a built-in MATLAB function. By converting each pixel's intensity to grayscale, one frequency spectrum was produced for each pixel whereas a RBG pixel would have produced three separate frequency spectra, one for each color. These spectra could not be combined mathematically to produce a single equivalent grayscale spectrum. The mean grayscale intensity was removed and one block of 4096 images was analyzed resulting in a frequency resolution, $\delta f$, of 18.31 Hz.

The dynamic pressure sensor data for each sensor was split into 36 blocks with quarter overlap of 4096 samples resulting in a $\delta f$ of 18.31 Hz. After determining the amplitude of the transformed pressure signal, the mean pressure amplitude was converted into sound pressure level using Eq. (2) [31].

$$\mathrm{SPL(f)} = 20\mathrm{Log}_{10}\left(\frac{\mathrm{Prms}}{\mathrm{P_{ref}}}\right) \tag{2}$$

where $P_{ref}$ was $2.0e^{-8}$ kPa.

Since the sample frequency and consequently the DFT doesn't have an ideal response characteristic with a bandwidth of 1 Hz the sound pressure level was converted to spectrum level.

## 3. RESULTS

Results in the first section will examine the high speed videos to qualitatively understand the changes that occur between the different flow control devices, i.e. approximate shear layer size and location, along with the two recirculation regions that are known to be observed in the cavity at this L/D ratio. The second section will consist of the discussion of the fluctuating pressures measured inside the cavity. The third and fourth sections will examine the side view and top view of the high speed videos, respectively to understand the differences between the observed flow fields.

### 3.1. Qualitative High Speed Video

Figure 6b shows the ridges device image and little difference between the baseline can be noticed. Figure 6c shows the flat spoiler image - a slight fuzziness is partly due to enlargement in order to match the scale of the other images. It can be seen that there is a shock off the flat spoiler and it does lift the

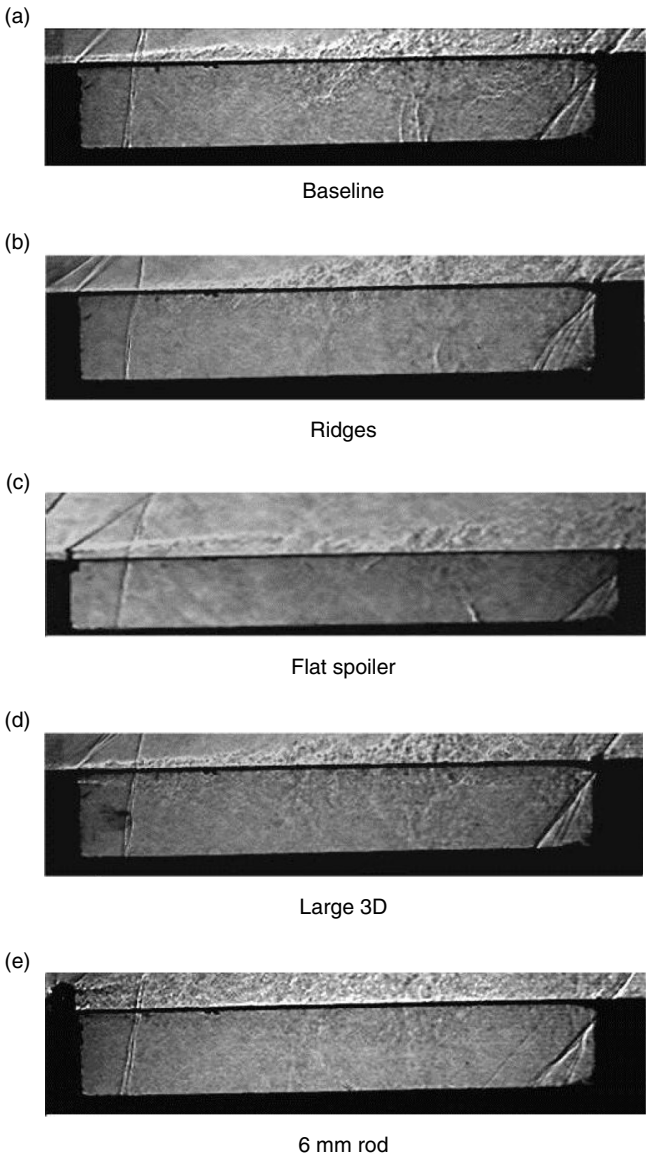


Figure 6. Shadowgraphs of the cavity flow at Mach 1.5, side view (a) Baseline, (b) Ridges, (c) Flat Spoiler, (d) Large 3D Backward Facing Steps, (e) 6 mm Rod. Flow is Left to Right.

shear layer. At this instant an aft-ward traveling acoustic wave is noticeable inside the cavity. Figure 6c shows the ridges device image and a slight difference between the baseline can be noticed. Again an aft-ward traveling acoustic wave was noticeable inside the cavity. Figure 6d shows the large 3D backward facing steps image. The streamwise vortices that are produced from the large 3D backward facing steps are noticeable below the leading edge of the cavity. In the high speed videos for the large 3D backward facing steps and the 6 mm rod no aft or forward traveling acoustic wave is observed. Schmit et al. [16] showed that in the baseline case, the observed forward and aft traveling waves occurred when the pressure inside the cavity was lower than the traveling pressure wave. As will be shown in the next section, the flat spoiler and ridges device have nearly the same pressure difference as the baseline case, e.g. the acoustic peaks are around 145 dB while the background is around 130 dB. The large 3D backwards facing steps and 6 mm rod have lower pressure differentials, acoustic peaks around 132 dB with a background around 128 dB, which result in no forward or aft travel pressure wave being observed for these two device. The Figure 6e shows the 6 mm rod image with a clearly visible wake, but without additional flow features.

Figure 7 shows the sketches of the observed flow field patterns from the side view for the various geometries tested. The dashed line ovals in Figure 7a – e are the forward recirculation regions that are present in the flow field, but are not observable in the shadowgraphs videos due to low density fluctuations in this region. Figure 7a describes the baseline flow field patterns. The main flow features that are depicted are the shear layer with distinct large vortices traversing the cavity. These features have been discussed in Schmit et al. [16] but included here for comparison purposes. Figure 7b shows the flow pattern for the ridges. The shear layer produces large scale vortical structures that are nearly the same size and strength as the baseline. Figure 7c shows the flow pattern for flat spoiler. The most noticeable difference is the fact that the shear layer is lifted upwards but retains similar vortical structures. Figure 7d shows flow pattern for the large 3D backward facing steps. The shear layer is significantly different in that the shear layer starts below the waterline of the cavity and slightly dips further into the cavity and then back out. No large scale vortices are noticed in the shear layer. The recirculation region in the aft of the cavity is about the same size in the side view. Figure 7e shows the 6 mm rod flow pattern. The side view flow pattern is the most transformed. Since the rod sheds it own vortices, the cavity shear layer is altered in such a way that no major vortices form inside the cavity's shear layer and a larger recirculation region in forward part of the cavity is formed.

Figure 8 shows five instantaneous images of the top view of the cavity at Mach 1.5, with flow from left to right. Figure 8a shows the baseline image and is again used for a comparison with other cases. One interesting observation in the baseline image is the aft-ward traveling wave that stretches across the entire cavity. Figure 8b, c, d, and e shows the flat spoiler, ridges device, large three dimensional backward facing steps and the 6 mm rod, respectively. In the top view most flow structures are not observable as compared to the side view, but by understanding how the flow control device changes the flow field, a better understand of the side view images can become more clear. The aft-ward traveling acoustic wave can be clearly observed in Figure 8c but all of the images have an acoustic wave in the images, except for the 6 mm rod.

Figure 9 is shows the inferred sketches of top views of the observable flow fields patterns for the various passive flow control devices tested. Figure 9a is the baseline flow field patterns and the bifurcated reticulating region is observable in the aft of the cavity. Again this feature has been discussed in Schmit et al. [16] and is included here for comparison purposes. Figure 9b shows the ridges device flow pattern and the bifurcated recirculation region is nearly the same size and strength as the baseline. Figure 9c shows the flat spoiler flow pattern and the bifurcated recirculation region again is nearly the same as the baseline case. Figure 9d shows the large 3D backward facing steps flow pattern and the recirculation region in the aft of the cavity looks a lot smaller in the top view. A new flow pattern is observed in the top view; the streamwise vortices that are formed from the large 3D backward facing steps are seen. Another

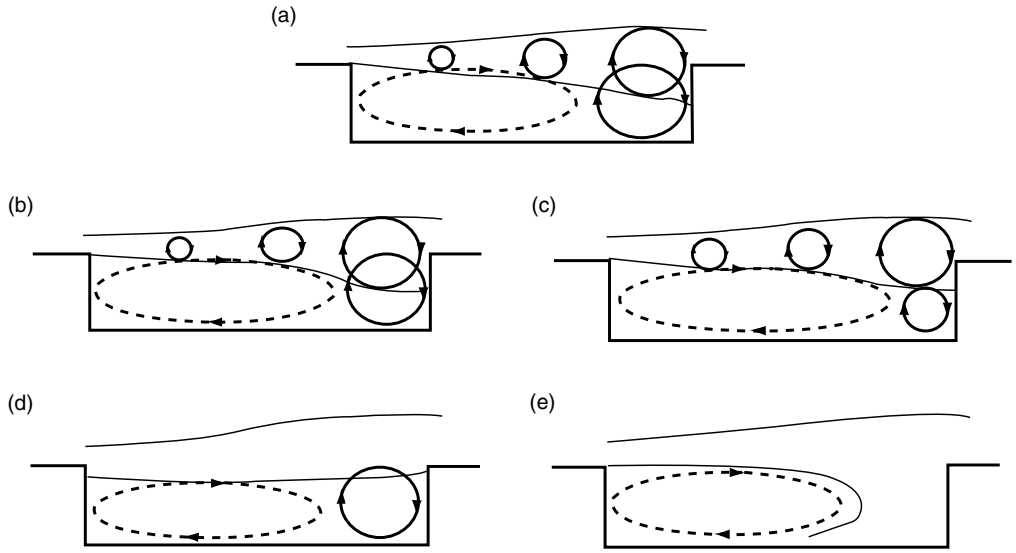


Figure 7. Inferred topology of the flow inside the cavity, side view. (a) Baseline, (b) Ridges, (c) Flat Spoiler, (d) Large 3D Backward Facing Steps, (e) 6 mm Rod. Flow is Left to Right.

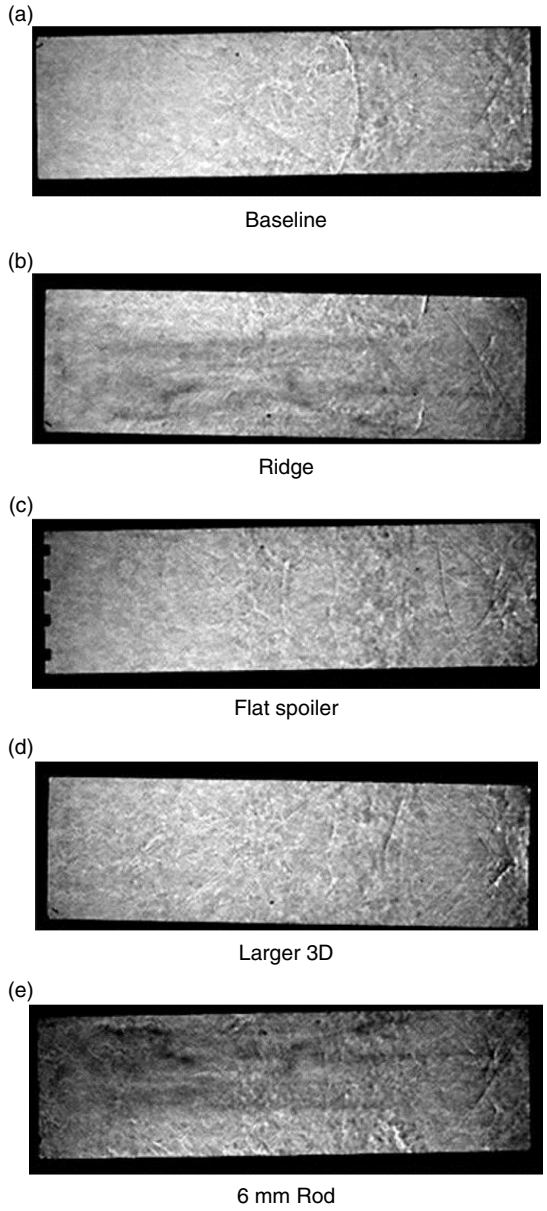


Figure 8. Shadowgraphs of the cavity flow at Mach 1.5, top view (a) Baseline, (b) Ridges, (c) Flat Spoiler, (d) Large 3D Backward Facing Steps, (e) 6 mm Rod. Flow is Left to Right.

pattern that is observed is the inflow from the outside of the cavity. Figure 9e shows the 6 mm rod flow pattern and the only major flow field pattern that is observable is the shedding from posts that hold the rod.

### 3.2. Pressure Data Analysis

Unless otherwise stated, three pressure sensor locations at x/L = 0.35, 0.80 and 1.00 will be used to examine the differences between the baseline cavity and the four flow control devices. Each of these locations was chosen for specific reasons. The x/L = 0.35 location examines the forward recirculation region, while the x/L = 0.80 location examines the aft recirculation region. The x/L = 1.00 location pertains to the aft wall of the cavity.

Figure 10 shows the acoustic spectrum at the aft wall of the cavity for all of the devices tested along with the baseline case. Though several additional flow control devices were tested at this condition the four that will be discussed in this paper show a performance extreme in the acoustic results and

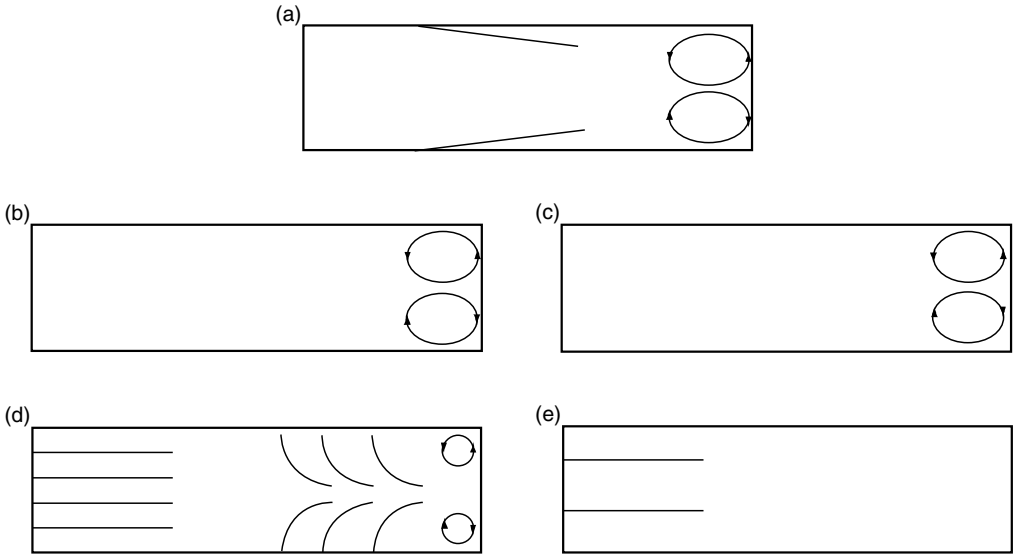


Figure 9. Drawings of the inferred flow structures inside the cavity, top view. (a) Baseline, (b) Ridges, (c) Flat Spoiler (d) Large 3D Backward Facing Steps, (e) 6 mm Rod.

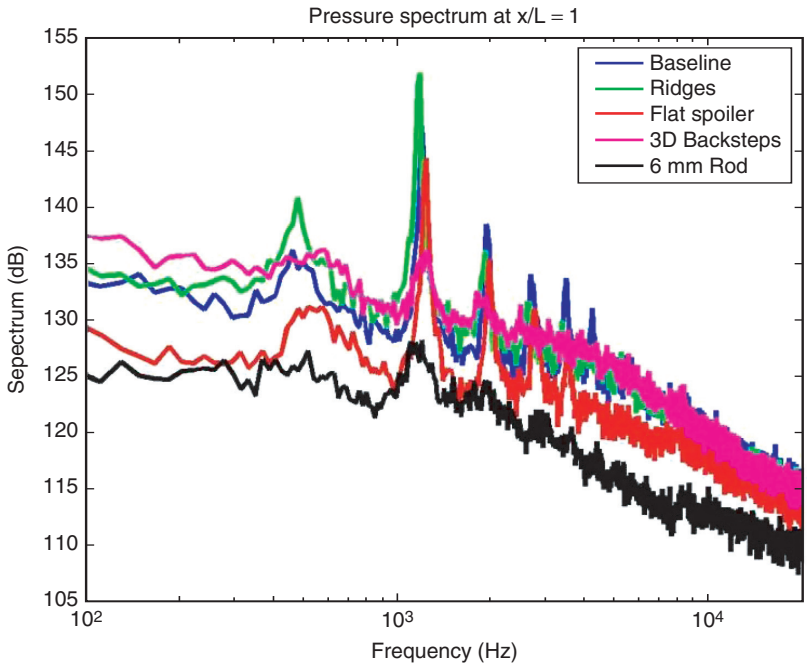


Figure 10. Aft wall pressure spectrum for various passive flow control devices.

therefore a detailed analysis on the effects to the flow physics will be discussed. The best geometry modifying device that reduced the acoustic tones and the broadband noise level the most was 6 mm rod with a 2.54 mm gap. The next best performing geometry modifying device was the large 3D backward facing steps. It was able to reduce the acoustic tone significantly, but slightly increased or maintained the broadband noise throughout the spectrum. The flat spoiler was able to reduce the broadband noise though it could not reduce the acoustic peaks to the broadband levels like the 6 mm rod. The ridges device on the other hand increased the broadband noise level, dramatically increasesed the acoustic tone and shifted the acoustic tone frequency down by 50 Hz. Table 2 shows the acoustic performance of each of the passive devices tested in comparison to the baseline.

Table 2. Comparison of acoustic tones and shifts

| Device | OASPL dB | Delta OASPL dB | Peak Frequency Hz | Peak Tone dB | Delta Peak Tone dB |
|---|---|---|---|---|---|
| Baseline | 157.09 | | 1190 | 147.5 | |
| Ridges | 158.15 | +1.06 | 1172 | 152.0 | +4.5 |
| Flat Spoiler | 153.92 | –3.17 | 1227 | 144.5 | –3.0 |
| Large 3D Step | 156.80 | –0.29 | 567.6 and 1227 | 136.4 | –11.1 |
| 6 mm Rod | 148.54 | –8.55 | 1154 and 1190 | 128.7 | –18.8 |

Since the frequency spectrum has been ensemble averaged, it tends to smooth the data and consequently, the information about the instantaneous excursions in pressure data are lost. Instead, the time histories can provide an insight into the effectiveness of the flow control devices. Figure 11 shows the time history of dynamic pressures for the three pressure sensors locations stated above for all of the cases tested. Figure 11a, b and c. are the pressure time traces for baseline case at x/L = 0.35, 0.80 and 1.00, respectively. Figure 11d, e, and f are the pressure time traces for the ridges case at x/L = 0.35, 0.80 and 1.00, respectively. Figure 11g, h, and i are the pressure time traces for the flat spoiler case at x/L = 0.35, 0.80 and 1.00, respectively. Figure 11j, k, and l are the pressure time traces for the large 3D backward facing steps case at x/L = 0.35, 0.80 and 1.00, respectively. Figure 11m, n, and o are the pressure time traces for the 6 mm rod case at x/L = 0.35, 0.80 and 1.00, respectively. The first observation about the pressure time traces in Figure 11 is the pressure levels difference between the sensor locations. The sensor located at x/L = 0.35 never experience an acoustic peak above 20 kPa

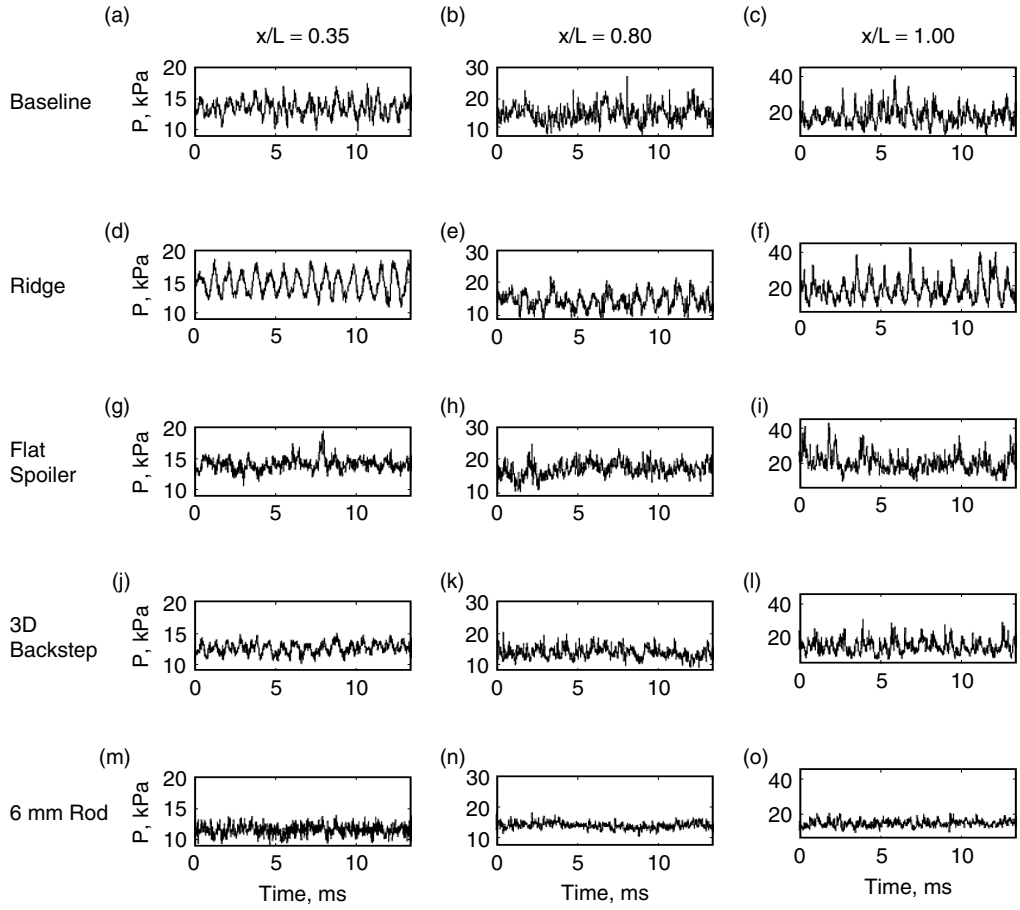


Figure 11. Pressure time traces. Left column: Sensor location x/L = 0.35, Middle column: Sensor location x/L = 0.80, Right column: Sensor location x/L= 1.00.

while the x/L = 0.80 sensor see acoustic peaks between 20 kPa and 30 kPa. The aft wall, x/L = 1.00, has acoustic peaks above 30 kPa which is expected since the aft wall experiences the highest dynamic pressure in the cavity. One noticeable difference between all of the time traces is in Figure 11d, the x/L = 0.35 sensor location with the ridges device. This time trace is the most sinusoidal of all sensors with nearly a 12 kPa peak-to-valley fluctuations. The flow control device with the most interesting pressure time trace is the 6 mm rod, Figure 11m, n and o, and they show that no acoustic peaks are present in the time traces as well as the fact that pressure levels are nearly the same throughout the cavity.

Additional insight into the physics of the flow encountered in the cavity for different geometries can be obtained by examining the probability density functions (PDF) of the pressure signals in Figure 12 shows the PDFs for the pressure sensors located at a. x/L = 0.35, b. x/L = 0.80 and c. x/L = 1.00. The PDFs at x/L = 0.35, in Figure 12a, are nearly Guassian except for the ridges and flat spoiler devices. As seen in Figure 11d, the ridges device is very sinusoidal and the pressure is not as random as turbulence would indicate. The flat spoiler's PDF indicates that the device narrows the pressure fluctuations at this location. The PDF's at x/L = 0.80, in Figure 12b, show that the pressure distribution is becoming skewed, mainly from the higher one-sided pressure spikes as indicated in the Figure 11. The baseline and ridges cases have narrower pressure fluctuations because of the stronger pressure spikes that occur in this section of the cavity. The other three devices are more Guassian even though they are slightly skewed. The PDF's at x/L = 1.00, shown in Figure 12c, are the most skewed results and are from the very high pressure spikes.

The level of skewness, or asymmetry of the PDF, and how it varies in the cavity is shown in Figure 13a. The skewness is relatively minor, levels below or near 0.1 for most of the forward recirculation region. The increase in skewness near the forward wall is potentially from the acoustic waves interacting with the forward wall and/or the flow field interacting with the corners of the cavity. William et al. [32] stated that skewness above 0.4 in jets creates crackle. The aft recirculation region and the aft wall of the cavity are above the skewness of 0.4 for all cases except the 6 mm rod. The objective of the present

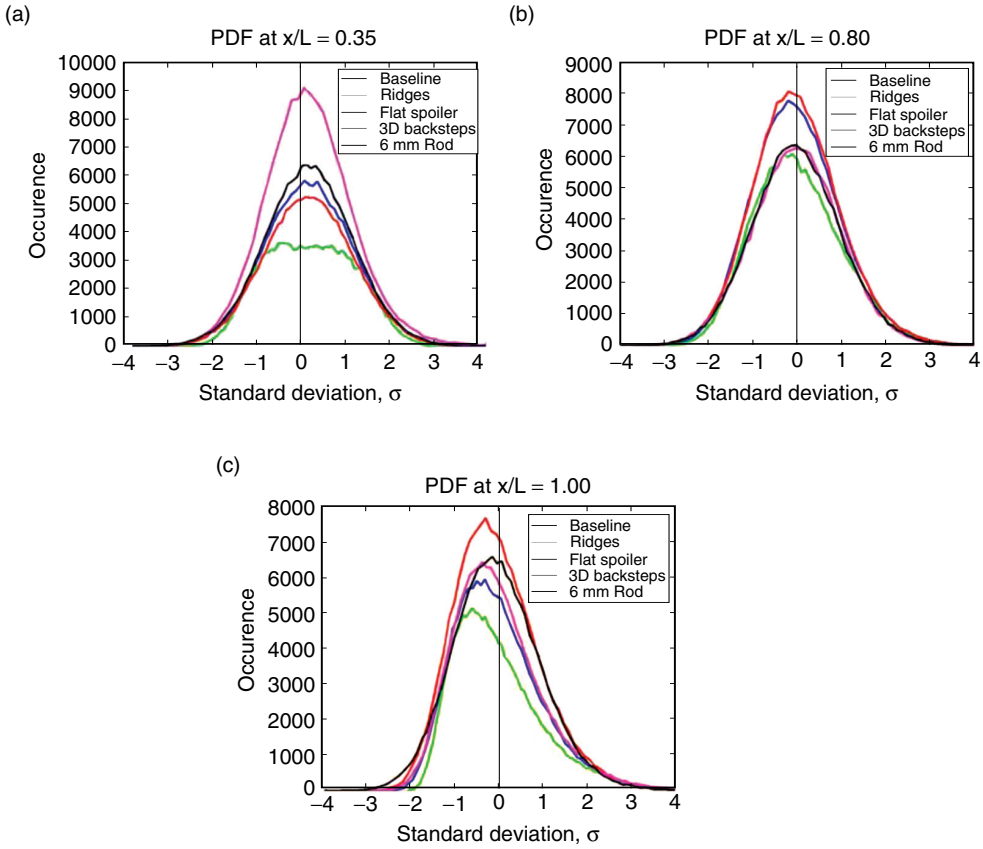


Figure 12. Probability Density Functions (PDF's) of the pressure data for the various flow control devices; (a) x/L = 0.35, (b) x/L = 0.80 and (c) x/L = 1.00.

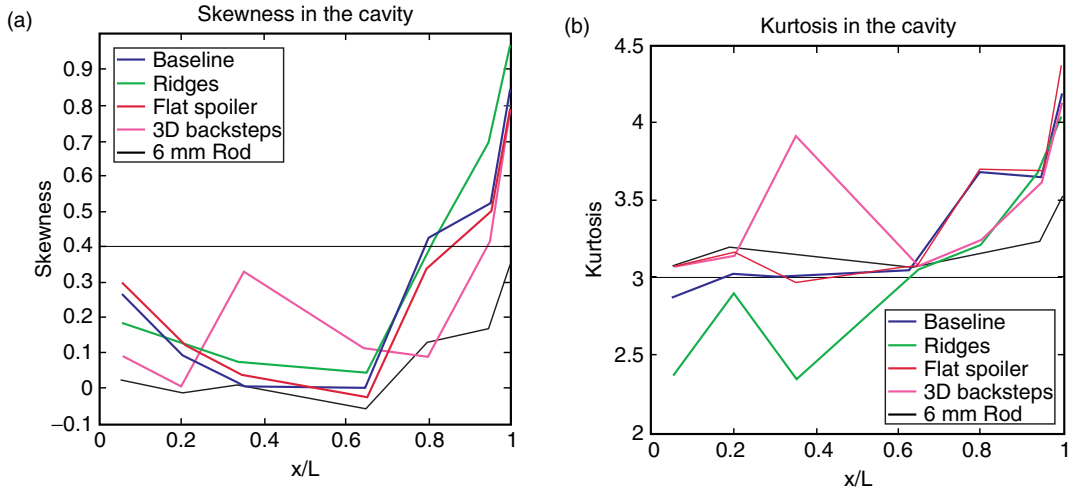


Figure 13. Pressure signals inside the cavity; (a) Skewness, and (b) Kurtosis.

work is not to determine whether or not crackle occurs in the cavity, but this does bring up an interesting problem that needs further investigation. One explanation as to why the skewness is so high in the aft section of the cavity is the fact that the entrained flow from the shear layer interacs with acoustic waves that are propagating throughout the cavity. Due to this interaction a very high pressure spike is produced and is evident in pressure traces of Figure 11. The reason why the skewness of 6 mm rod does not rise above the 0.4 level is because the rod does not allow for coherent entrainment of freestream fluid into the cavity which results in the reduction in the formation of acoustic waves in the cavity.

Figure 13b is the kurtosis, or sharpness to the PDF peak, of the pressure data inside the cavity. A level of 3 indicates a Gaussian profile; a level below 3 indicates the profile is flatter than a Gaussian profile, while level above 3 indicates the profile is narrower than a Gaussian profile. Again the forward recirculation region has a nearly Gaussian profile except for the ridges and the flat spoiler. As one observes the pressure time trace for the ridges device, Figure 11d, the forward recirculation region becomes sinusoidal which in turn will produce a flatter profile because the pressure distribution is very periodic. As for the flat spoiler, examining the pressure time trace, Figure 11g, shows that the sensor sees a very narrow range of pressure fluctuations that have some slight periodicity. The aft recirculation region and the aft wall have a narrower profile because the shear layer and the acoustic waves inside the cavity are very repetitive and therefore produce a very narrow, but high pressure frequency spectrum.

Figure 14 shows the autocorrelation for each of the three pressure sensors examined for all the flow modifying devices tested. Figure 14 a, b and c. are for the pressure sensor at x/L = 0.35, 0.80 and 1.00, respectively. As one notices that the autocorrelation for the baseline, ridges and the flat spoiler devices is sinusoidal and does not decay to zero which indicates that these flow fields are not stationary [33], but very periodic which is expected. The ridges device is the most correlated, the autocorrelation coefficient peaking nearly ±0.8, and is from the single peak tone that this present in the cavity. As for the large 3D backward facing steps and the 6 mm rod, the autocorrelation shows that both devices quickly decay toward zero, but still have some periodicity in the forward and aft recirculation regions (Figure 14a, b) while the aft wall sensor slowly decays to zero.

Presented in Figure 15 is the cross correlation between each of the pressure sensors. Figure 15a is the cross correlation between pressure sensor located at x/L = 0.35 and with the sensor located at 1.00 for all configurations. Figure 15b is the cross correlation between x/L = 0.80 and 1.00 for all configurations. Figure 15a shows that the forward recirculation region is initially out-of-phase with the aft wall and then starts to periodically cycle. Figure 15b shows the aft recirculation region is initially in-phase with the aft wall and again starts to periodically cycle though correlation is not as great as the forward recirculation region. Figure 15c is the cross correlation between x/L = 0.35 and 0.80 for all configurations and they are initially out of phase and go into a periodic cycle. By examining the cross correlation differences between Figure 15c confirms that there are two recirculation regions in the cavity that do cross talk depending on the strength of acoustic waves that traverse the cavity. Since the

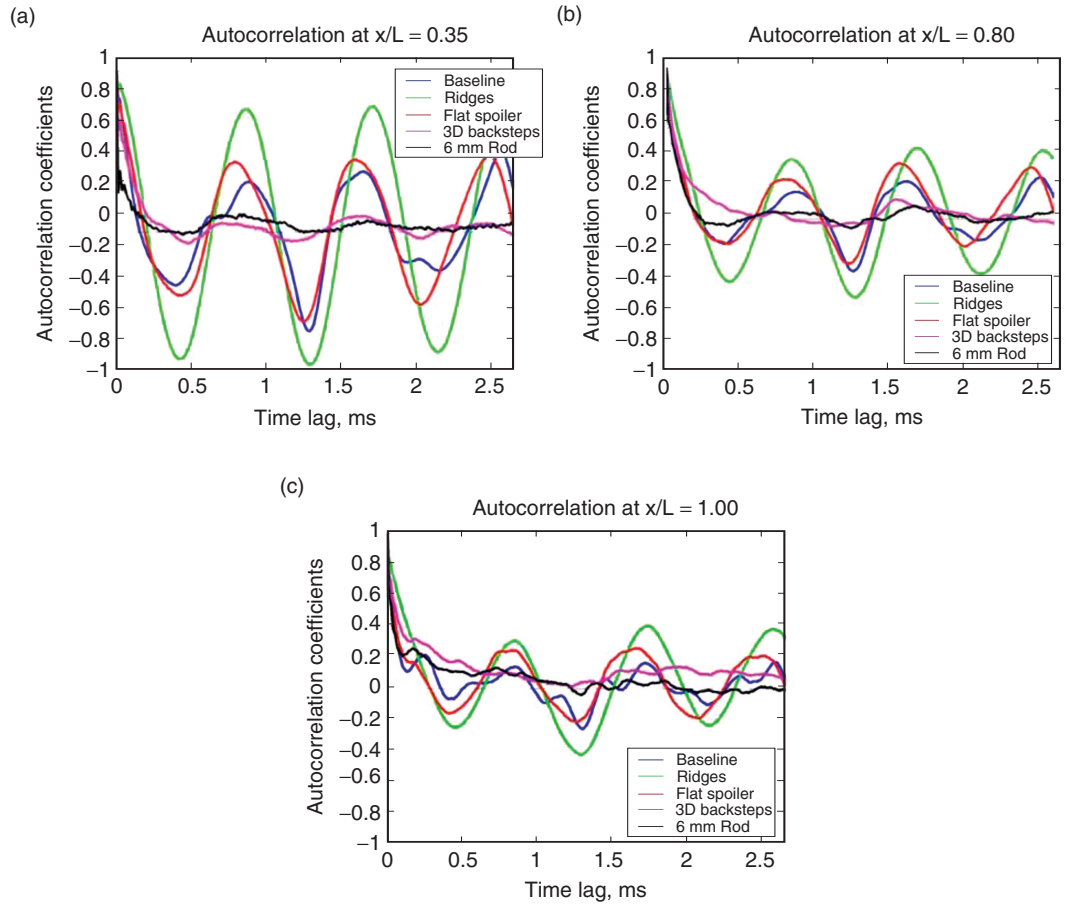


Figure 14. Autocorrelation of the pressure sensor signals. (a) x/L = 0.35, (b) x/L = 0.80 and (c) x/L = 1.00.

device with ridges has a single dominant tone the cross correlation is significantly higher than the baseline while the flat spoiler cross correlation is nearly the same as the baseline. With the large 3D backward facing steps there is virtually no correlation between any of the sensors which is indicative of a large recirculation region in the front of the cavity. As with the larger 3D backward facing steps, there is virtually no correlation between any of the sensors because of the larger recirculation region that spans most of the cavity.

Figure 16 shows the instantaneous pressures throughout the cavity. The black vertical lines indicate the sensor locations and no data is plotted from x/L = 0.0 to 0.05. Since the dynamic pressure sensors are at discreet locations, the MATLAB plotting routine stretches the pressure values throughout the cavity. One feature that is noticeable is the pumping action in the cavity which is higher pressure fluid traveling upstream inside the cavity. Figure 16a is the baseline case and shows the cavity is driven by the pumping action. Schmit et al. [16] give more detail about the pumping action inside the cavity. Figure 16b shows that the pumping action with the ridges is slightly more noticeable with this device indicating that the vortices are slightly stronger when they penetrate the cavity. Figure 16c is the flat spoiler and the pumping action is not as prevalent as the baseline case. Figure 16d is the large 3D backward facing steps and the pressure fluctuations are not as great throughout the cavity since no vortices are being formed to penetrate the cavity depths to create the pumping action. Figure 16e is the 6 mm rod and the pressure fluctuations are not as great throughout the cavity since no large scale vortices are being formed even though they are penetrating the cavity.

Figure 17 shows the pressure spectrum along the ceiling of the cavity. Figure 17a shows the baseline pressure spectrum and the peak frequency is dominate throughout the cavity though it dips slightly near the front wall. Other acoustic peak frequencies are present as well throughout the cavity. Figure 17b shows the ridges device and the peak frequency is dominate throughout the cavity with a dip near the leading edge. Most of the other frequencies that are present in the baseline are not as strong and

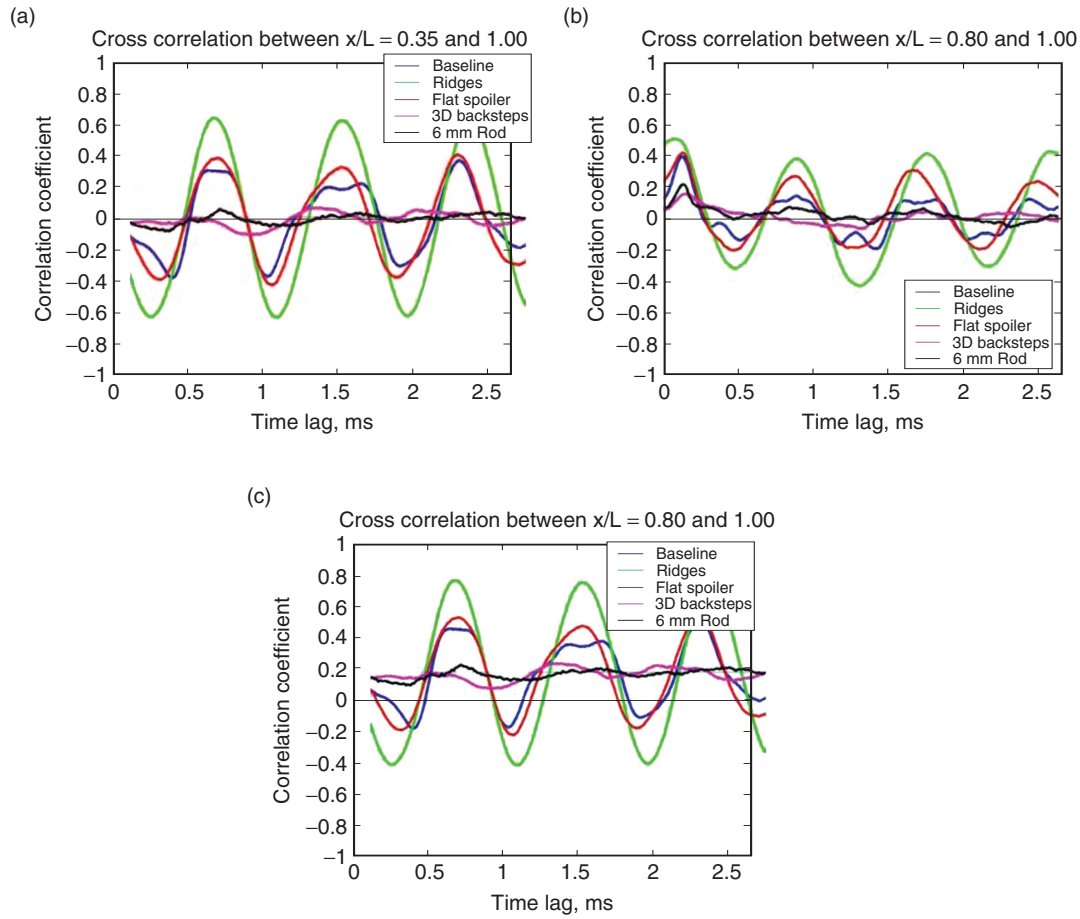


Figure 15. Cross correlation between the pressure sensors. (a) Correlation between x/L = 0.35 and 1.00, (b) Correlation between x/L = 0.80 and 1.00, (c) Correlation between x/L = 0.35 and 0.80.

therefore not as noticeable. Figure 17c shows the flat spoiler and the peak frequency is dominate throughout the cavity. Most of the other frequencies are present like the baseline showing that the flat spoiler is not effective of lifting the shear layer over the entire cavity. Figure 17d shows the large 3D backward steps and the peak frequency in the ceiling of the cavity is not at the dominant frequency that has been observed with all other devices so far. The peak frequency is around 200 Hz which indicates the some other flow feature is creating the acoustic peak since it doesn't traverse the entire cavity. Figure 17e shows the 6 mm rod and the peak frequency at the ceiling of the cavity is not at the dominant frequency observed with all other devices but is around 200 Hz which indicates larger recirculation region.

### 3.3. Qualitative Side View Shadowgraph Results

In this section the high speed shadowgraph images for the side view of the cavity are examined. Although the shadowgraph results are based on the integrated optical pathway of density fluctuations it is still important to understand the physical changes that occur within the cavity using this technique. For most of this section, three pixel locations will be examined, x/L = 0.50, z/D = +0.01; x/L = 0.99, z/D = +0.01; x/L = 0.99, z/D = –0.50, for all flow control device tested, unless otherwise stated. The first two locations represent two point in the shear layer just above the waterline of the cavity, and this will provide some perspective in how the shear layer develops over the cavity. The third location represent a point just upstream of the aft wall pressure sensor location and examining this location will result in a better understanding of the aft recirculation region, in addition to the interaction of the shear layer with the aft wall.

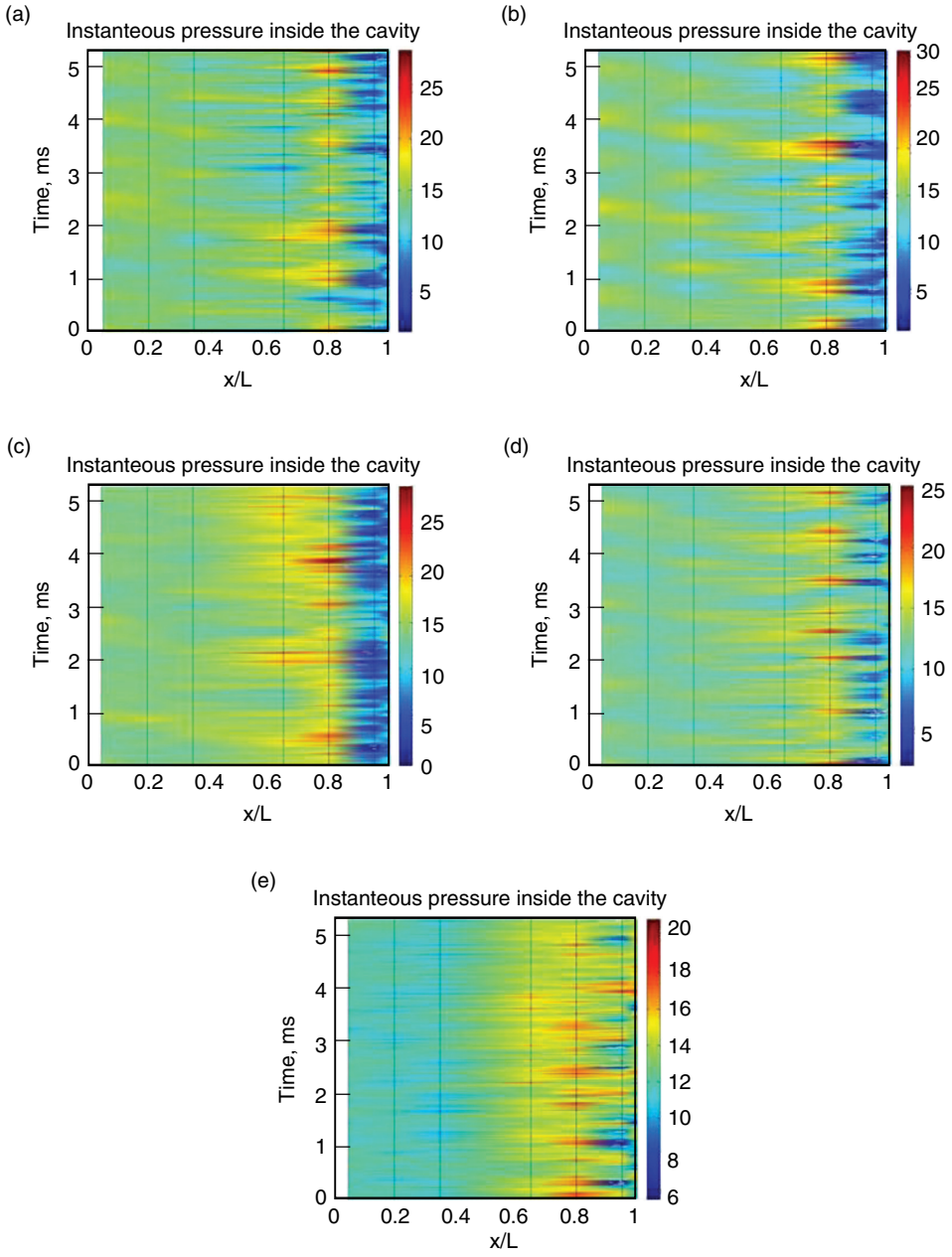


Figure 16. Instantaneous pressure in the cavity (a) Baseline, (b) Ridges, (c) Flat Spoiler, (d) Large 3D Backward Facing Steps, (e) 6 mm Rod.

Figure 18 shows the pixel intensity time traces for the three pixel locations stated above for each of the geometry modifications devices tested. A value of 0 indicates a color of black in the movies while a value of 256 indicates a color of white, for most of the movies the pixel intensity is on the darker side because the contrast and brightness were adjusted to provide optimal viewable resolution for the human eye. Figure 18a, b and c. are the pixel intensity time traces for baseline case at the three observed pixel locations, respectively. Figure 18d, e, and f are the pixel intensity time traces for the ridges case at the three observed pixel locations, respectively. Figure 18g, h, and i are the pixel intensity time traces for the flat spoiler case at the three observed pixel locations, respectively. Figure 18j, k, and l are the pixel intensity time traces for the large 3D backward facing steps case at the three observed pixel locations, respectively. Figure 18 m, n, and o are the pixel intensity time traces for the 6 mm rod case at the three observed pixel locations, respectively.

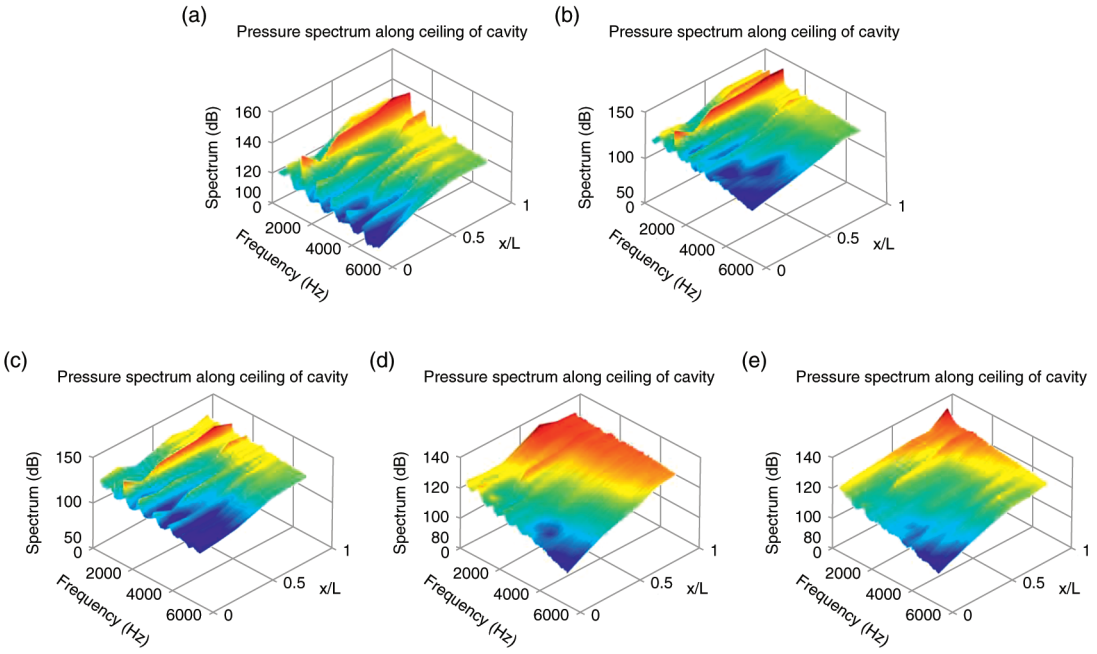


Figure 17. Pressure spectrum along the ceiling of the cavity (a) Baseline, (b) Ridges, (c) Flat Spoiler, (d) Large 3D Backward Facing Steps, (e) 6 mm Rod.

In the first location (left column in Figure 18) it is apparent that there are intensity spikes that go to the black side of the grey scale spectrum, which indicates a very strong density fluctuations in the shear layer which is produced either from very small but strong eddies in the shear layer or the two-dimensional entrainment of fluid into the shear layer. This same effect can produce a similar spike toward the white side of the grey scale which is also observed in the same column. The last two columns in Figure 18 are darker mainly due to the slight unevenness of the light source for the shadowgraph setup. When the middle column does go to black it usually represents the initial formation of the forward traveling acoustic wave. Figure 18e, the ridges device, shows the most periodic signal for all the conditions shown and is probably from the constant shedding and formation of vortices in the shear layer. Figure 18's right column is mainly the flow down the aft wall which is a combination of the aft recirculation region and the destruction of the shear layer at the aft wall. From the high speed shadowgraph video's, the relatively small black spikes are mostly the forward traveling acoustic waves, while the larger spikes on the white side are from the aft traveling acoustic waves inside the cavity interacting with the aft wall.

As for the flow control devices, the baseline, Figure18a-c and the ridges devices, Figure 18d-f, produce large two dimensional vortices that domain the shear layer and therefore have very similar characteristics. Since the flat spoiler, Figure 18g-i, lifts the shear layer, the large scale vortices do not form until much later in the cavity and is one reason why Figure 18g is relatively quite as compared to the other device at this location. The large 3d backward facing steps do not produce the large scale two dimensional vortices but the shear layer is more turbulent due to the smaller eddies inside the shear layer. The 6 mm rod produces a relatively thick wake / shear layer which initially contains smaller energetic eddies and through dissipation these eddies reduce in strength as they traverse downstream in the shear layer.

Figure 19 shows the PDF's of the pixel intensity from the previous time traces for all three locations and geometry modifying flow control devices for only 4096 images. Because of the limited number of samples and low quantization level of the grey scale image, the pixel intensity's PDF profiles are not as smooth as the pressure sensor's PDF profiles, but they can provide general trend to gauge the usefulness of the high speed shadowgraph movies. Figure 19a shows the PDF for the pixel location x/L = 0.50, z/D = +0.01 and shows that the profiles having a best Gaussian looking profiles out of the three locations. All the devices except the large 3D backward facing steps have the nearly the same profile. Figure 19b shows the PDF profiles for the pixel location x/L = 0.99, z/D = +0.01 and these profiles have less Gaussian looking profiles. The sharp increase in the profile below $\sigma = -1$ for the large 3D backward facing steps is probably created when shadowgraph signal goes black in the grey scale which can be seen

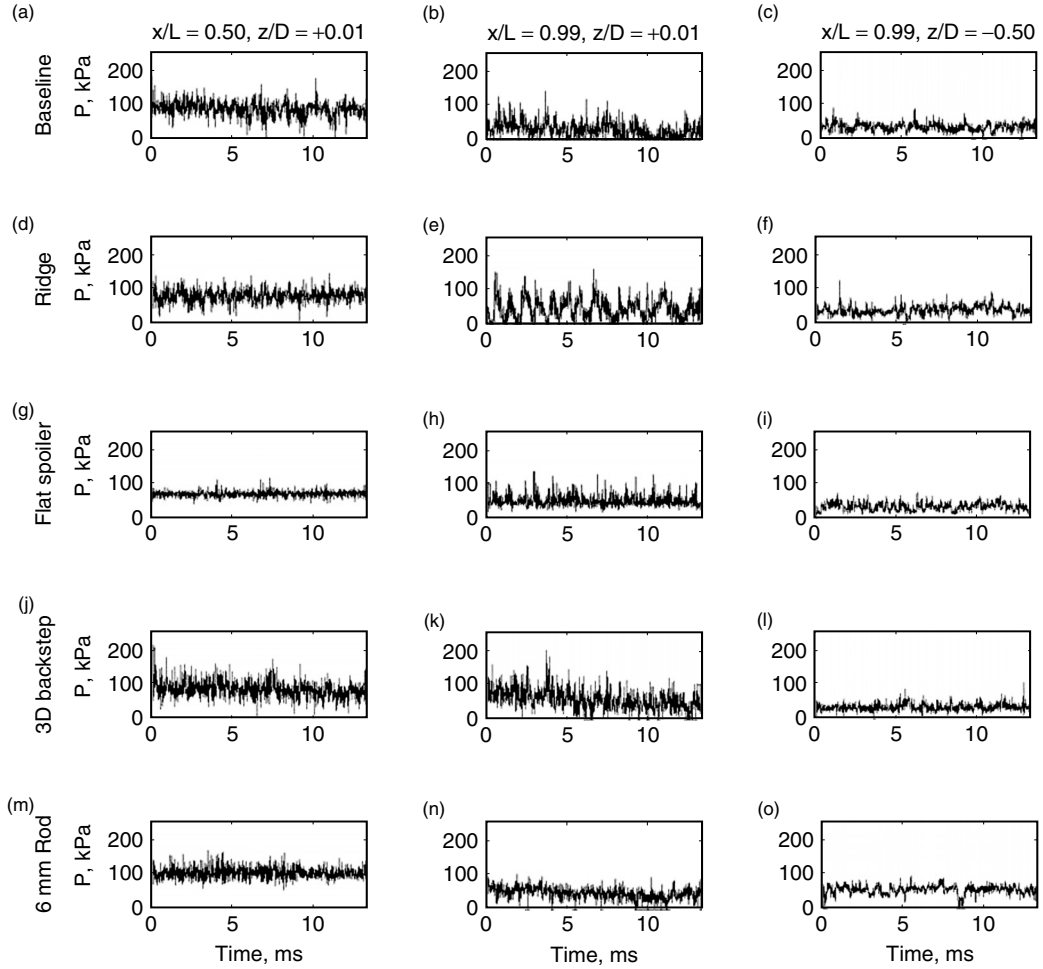


Figure 18. Time history of the shadowgraph pixel intensity. Left column: Pixel location x/L = 0.50, z/D = +0.01, Middle column: Pixel location x/L = 0.99, z/D +0.01, Right column: Pixel location x/L= 0.99, z/D = –0.50. First Row: Baseline, Second Row: Ridges, Third Row: Flat Spoiler, Fourth Column: 3D Large Backward facing steps, Fifth Row: 6 mm Rod.

in Figure 18k. Figure 19c is the PDF for the pixel location x/L = 0.99, z/D = –0.50 and again the baseline, ridges and flat spoiler's profiles all sharply increase below $\sigma = -1$ for the same reason above. One possible solution is to improve these profiles with improved evenness of the light across the cavity.

Figure 20a shows the skewness of the shear layer for five x locations at z/D = +0.01. The horizontal line at 0.4 skewness is just an indicator as to how much skewness is in the shadowgraph images. As one can see, the flat spoiler has the least amount of skewness in the shear layer as a result of the lifting. Figure 20b shows the skewness inside the cavity for five locations at z/D = –0.50. The 6 mm rod has the highest amount of skewness throughout much of the cavity, while the other flow control and baseline cases keep the skewness below 0.4. The 6 mm rod, which had the least amount of skewness on the ceiling of the cavity, as shown in Figure 13a, has one of the highest amounts of skewness throughout the shear layer. This variation in skewness could be from the fact that the 6 mm rod sheds smaller energetic eddies above the waterline of the cavity and these smaller eddies produce high frequency fluctuations which results in an increase in the skewness at x/L = 0.75. At the aft wall for the 6 mm rod, the skewness drops to the lowest level of all device which indicates that the small energetic eddies above the waterline have a lower intensity as a result of the higher energetic eddies entrained in the recirculation region.

Figure 21a shows the kurtosis of the shear layer at five x locations z/D = +0.01. The baseline and ridges case are nearly Gaussian throughout the shear layer, whereas, the flat spoiler and large 3D backward facing steps are non-Gaussian at the front of the cavity and become Gaussian at the rear of the cavity. The 6 mm rod is the worst in that it's non-Gaussian until x/L = 0.80 and then starts to go the other

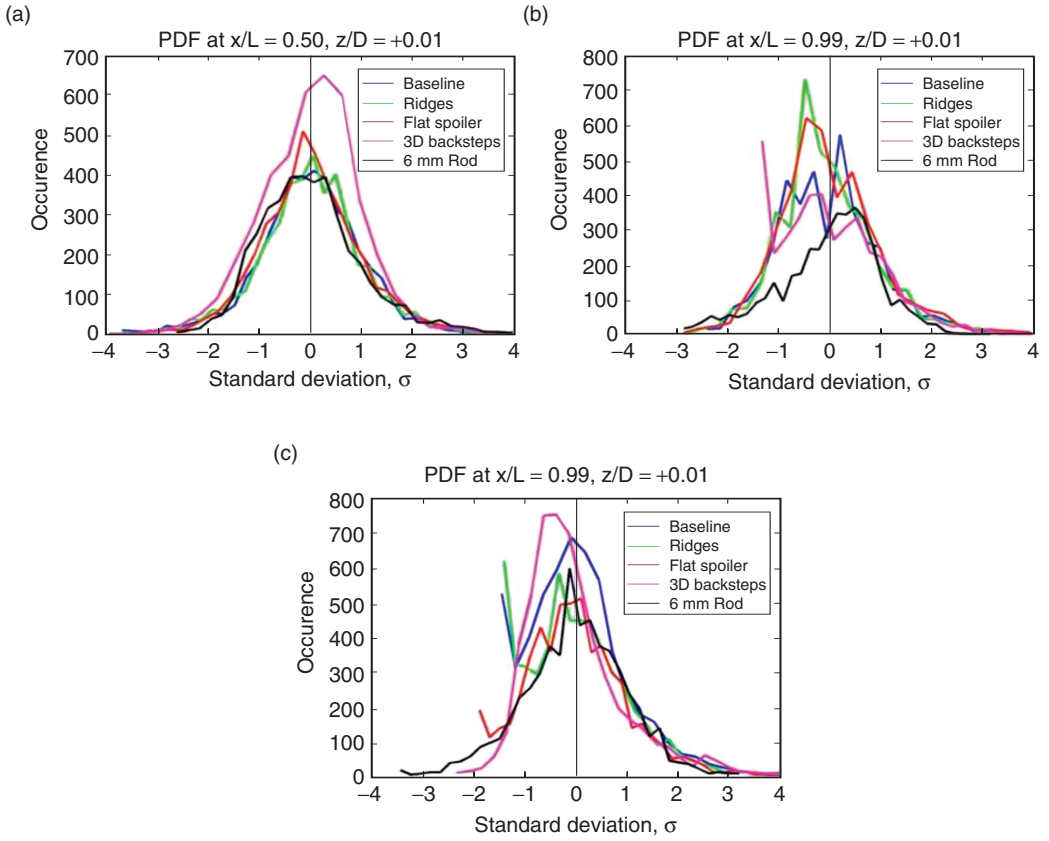


Figure 19. Probability Density Functions (PDF) of shadowgraph pixels intensity at, (a) x/L = 0.50, z/D = +0.01, (b) x/L = 0.99, z/D = +0.01 and (c) x/L = 0.99, z/D –0.50.

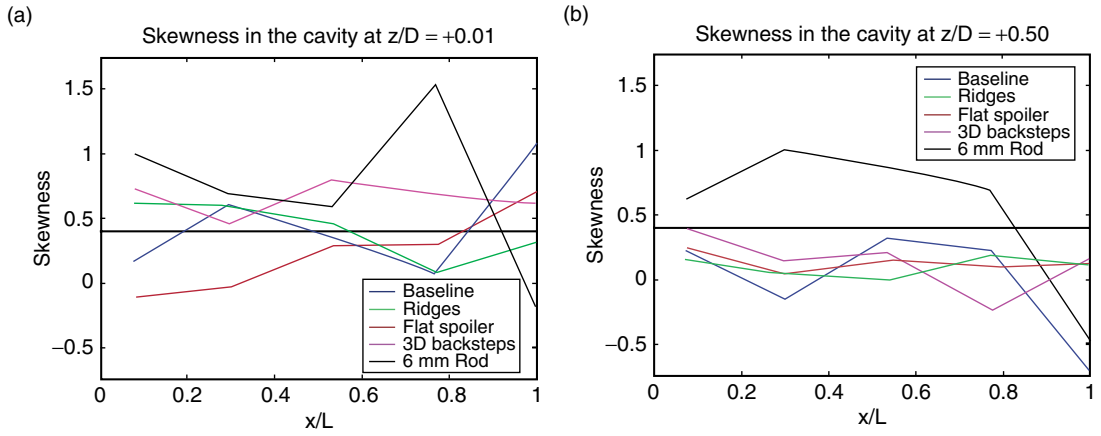


Figure 20. Skewness of the shadowgraph pixel intensity, side view; (a) z/D = +0.01, (b) z/D = –0.50.

way at the rear wall of the cavity. Figure 21b shows the kurtosis inside the cavity at five location at z/D = –0.50. The baseline case is the closest to being Gaussian in the cavity. The increase in Kurtosis at x/L = 0.75 for the 6 mm rod, flat spoiler and large 3D backward facing steps is probably do to the fact that this location is between the two recirculation regions and has a high amount of density fluctuations.

Figure 22a shows the autocorrelation for the pixel location at x/L = 0.50, z/D = +0.01. Since the baseline, ridges and flat spoiler devices produce large scale vortices inside the shear layer, the time lag for the first zero crossing of the autocorrelation coefficient, where the flow field will become uncorrelated with itself, is 0.267, 0.2, and 0.44 ms respectively. This indicates that several vortices pass

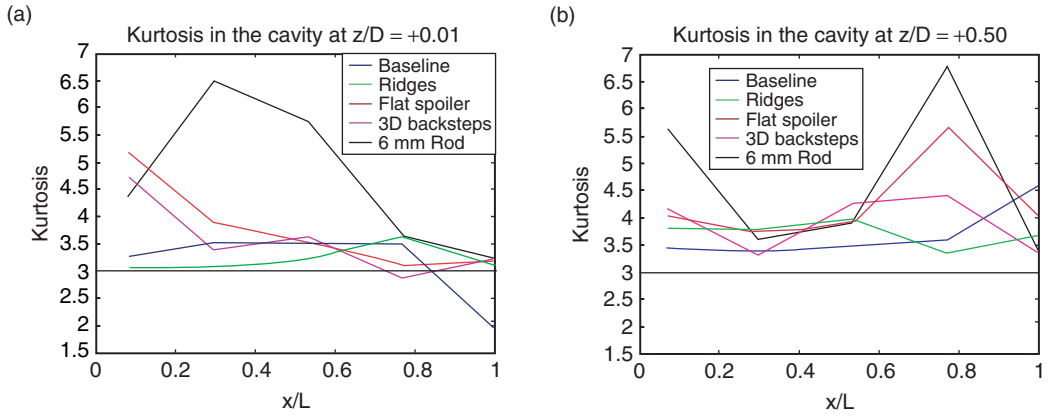


Figure 21. Kurtosis of the shadowgraph pixel intensity, side view, (a) z/D = +0.01, (b) z/D = –0.50.

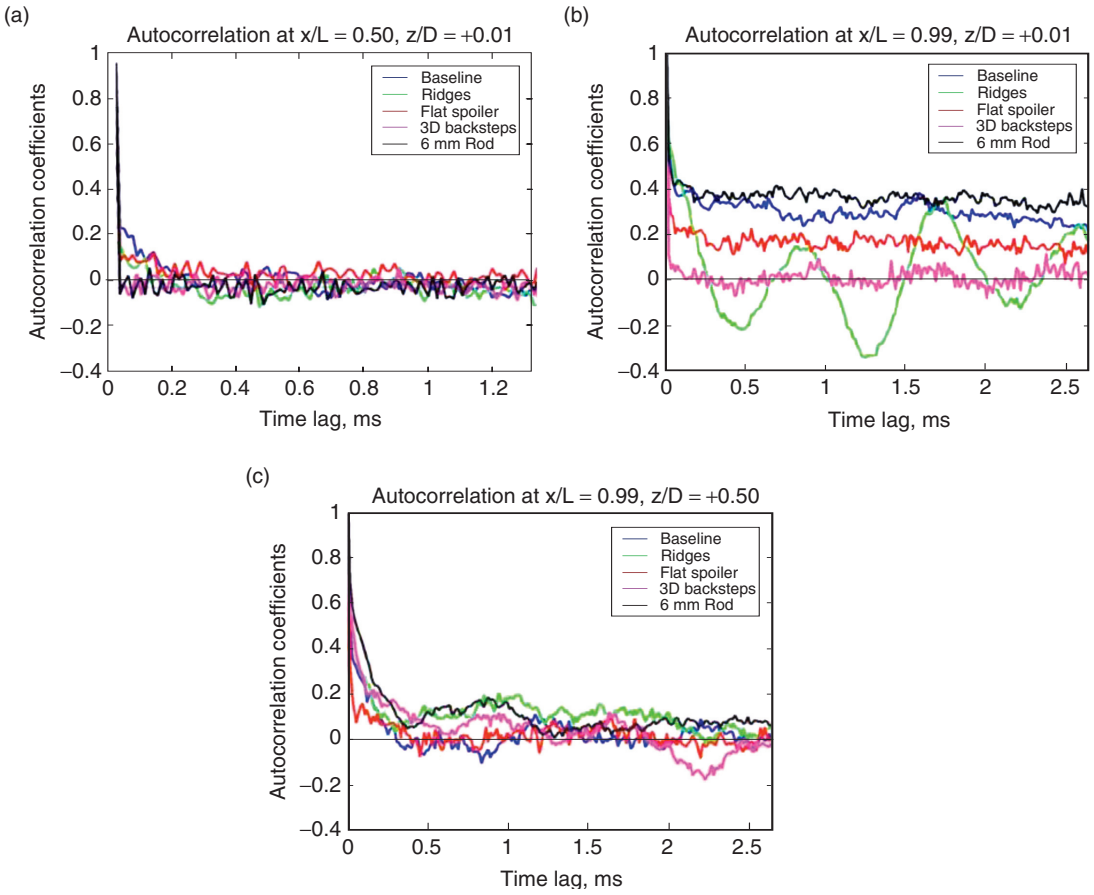


Figure 22. Autocorrelation of the shadowgraph pixel intensity for all cases, side view, (a) x/L = 0.50, z/D = +0.01, (b) x/L = 0.99, z/D = +0.01 and (c) x/L = 0.99, z/D –0.50.

this pixel location before it becomes uncorrelated with itself, but as with the pressure sensors shown in Figure 14, the flow field does not become stationary[33] as the coefficients do not decay to zero mainly due to the repetitive nature of the cavity flow [33]. The large 3D backward facing steps and 6 mm rod becomes uncorrelated rater quickly after a short time lag of 0.013 ms because they do not produce large scale vortices at this location. Figure 22b shows the autocorrelation for the pixel location x/L = 0.99, z/D = +0.01. The baseline, flat spoiler and 6 mm rod show an unusual autocorrelation coefficient plot in that they do not decay or oscillate around zero. On examining the movies for this location, a strong

density gradient is observed on the aft corner of the cavity and since this density gradient can extent upstream for several pixels, which depend on the instantaneous stagnation pressure, and results in a strong autocorrelation for these conditions. The ridges and large 3D backward facing steps have a strong stagnation density gradient but it is not observed with these devices because the stagnation density gradient does not extend upstream far enough to be sampled. Therefore, the autocorrelation is similar to the aft wall pressure sensors shown in Figure 15c. Because the ridges device produces a very periodic flow field, the autocorrelation decays to a periodic signal, while the large 3D backward facing steps decay closer to zero, but still has a slight periodicity. Figure 22c shows the autocorrelation for the pixel location x/L = 0.99, z/D = –0.50. Since this pixel location is just upstream of the pressure sensor, Figure 14c, it is not surprising that the both autocorrelations have similar characteristics. The baseline, ridges and flat spoiler in both figures have a time lag of around 0.4 ms when they cross the zero coefficient line. This shows that similar structures are being observed in the movies as well as in the pressure data. The large 3D backward facing steps along with the 6 mm rod again have trends similar to those presented in Figure 14c, in that they have a longer time lag before the near zero coefficient condition.

Figure 23a shows the cross correlation between the pixel locations x/L = 0.50, z/D = 0.01 and x/L = 0.99, z/D = 0.01. Since these two locations are both inside the shear layer, and are less than half the length of the cavity apart, the cross correlation is relatively strong and similar for all configuration tested. One would expect that these two locations would have a stronger correlation but several factors may affect this, e.g. shear layer growth, shear layer-aft wall interaction, and integrated optical path in a 3D flow field. Figure 23b shows the cross correlation between the pixel locations x/L = 0.50, z/D = 0.01 and x/L = 0.99, z/D = –0.50. As for this set of pixel locations, the cross correlation coefficients are really weak but as one will notice they do fluctuate periodically as the time lag increases. This does show that there is some correlation which is expected since the shear layer does interact with the aft wall but again the aft wall also sees a bifurcated aft recirculation region and acoustic wave interaction, as well as and the shear layer

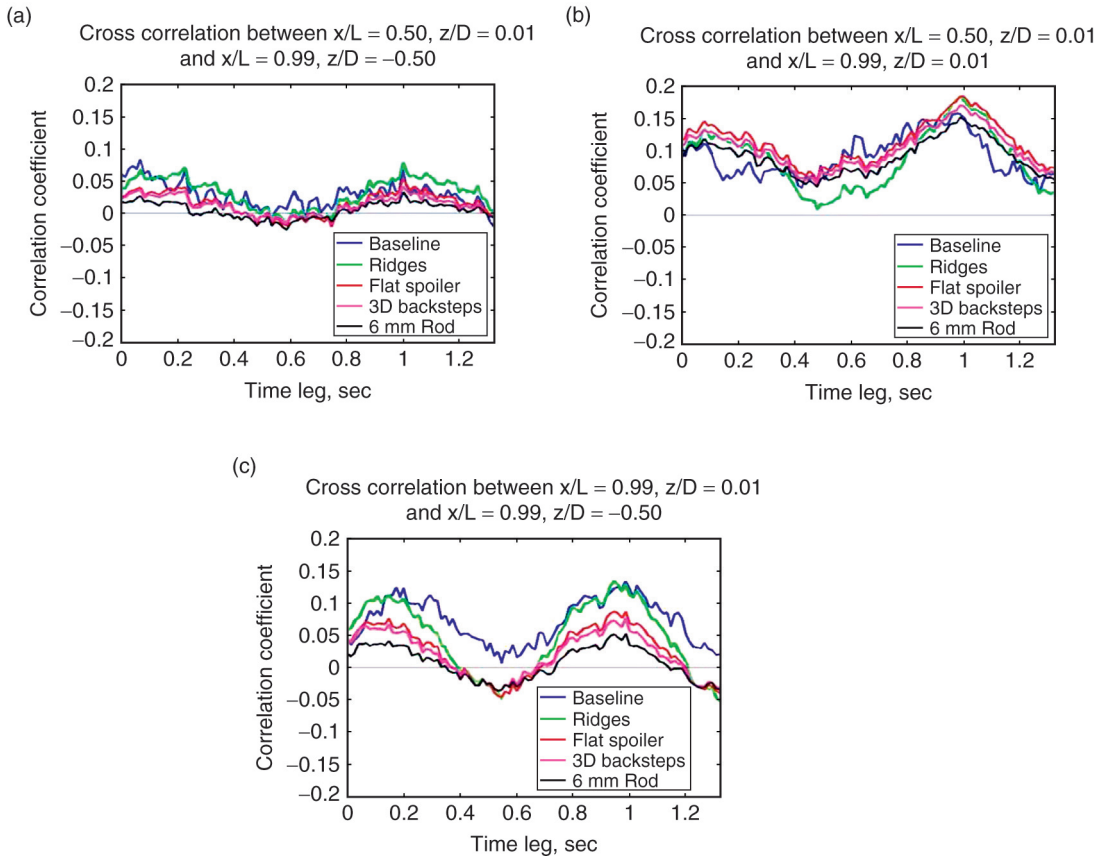


Figure 23. Cross correlation of the shadowgraph pixel intensity, (a) Correlation between x/L = 0.50, z/D = +0.01 and x/L = 0.99, z/D –0.50. (b) Correlation between x/L = 0.50, z/D = +0.01 and x/L = 0.99, z/D = +0.01, (c) Correlation between x/L = x/L = 0.99, z/D = +0.01 and x/L = 0.99, z/D –0.50.

entrainment interaction at this location which can reduce the cross correlation coefficients. Figure 23c shows the cross correlation between the pixel locations x/L = 0.99, z/D = 0.01 and x/L = 0.99, z/D = –0.50. This set of pixel locations has higher cross correlation coefficients because they are both near the aft wall of the cavity. Even thought they might not see the same flow features as stated above, there is enough similarity between these two locations to produce a relatively strong cross correlation.

Figure 24 shows the DFT results of the high speed shadowgraph images for the side view of the cavity. Figure 24a show the DFT results for the baseline case at 1190 Hz and is used for comparison purposes. See Schmit et al. [16] for more details on the baseline. The results show that at the peak acoustic frequency, the shear layer is the dominant feature in the flow field. The shocks have significant strength except they vary little across the spectrum unlike the shear layer. Figure 24b show the results for the ridges device and clearly indicate that at the peak acoustic frequency, the shear layer is the strongest feature in the flow field, though not as strong as the baseline. Figure 24c shows a zoomed out

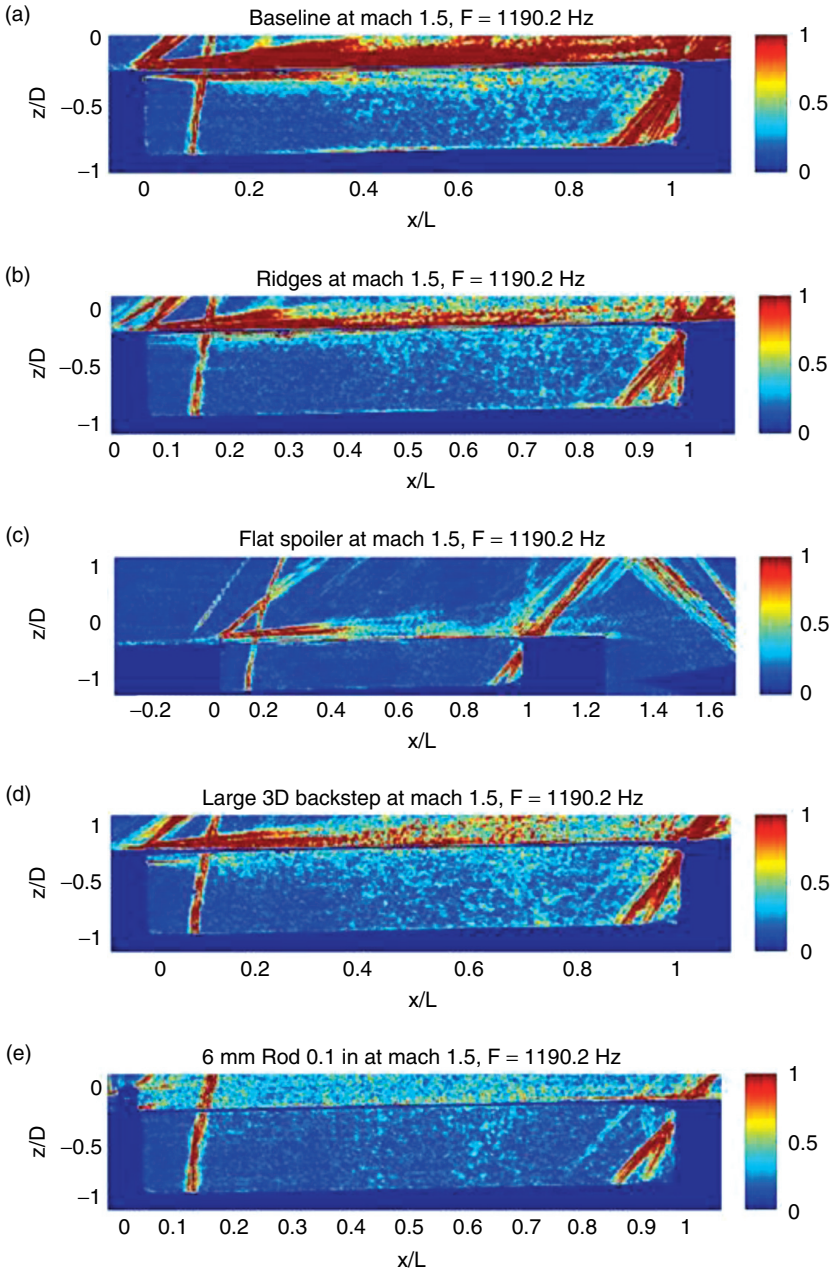


Figure 24. DFT of the shadowgraph images at 1190.2 Hz, side view; (a) Baseline, (b) Ridges, (c) Flat Spoiler, (d) Large 3D Backward facing steps and (e) 6 mm Rod.

image the results for the flat spoiler. Even though Figure 24c is zoomed out, the flat spoiler results show a similar trend in that the shear layer is the strongest feature in the flow field but it is not as strong as the baseline. Figure 24d show results for the large 3D backward facing steps. The side view once again shows that the shear layer is the strongest feature in the flow field but not as strong as the baseline. Figure 24e shows the results for the 6 mm rod and a weakened shear layer is clearly visible.

By analyzing the DFT results one can approximate the shear layer growth rate for each of the devices. Since the shear layer growth rate below the water line of the cavity is not well featured, only the top half is considered noting that the spread angle is a combination of shear layer growth rate and the normal mode due to hydrodynamic pumping. Since the hydrodynamic pumping action is relatively small near the leading edge of the cavity, the vertical displacement of the shear layer is relatively small, therefore the angle that is measured is assumed to be shear layer growth rate angle. The baseline shear layer growth rate angle, which is determined from the leading edge of the cavity, is approximately 18.5°. Note that Figure 24 is not to scale. The shear layer growth rate angles for the ridge device, flat spoiler and large 3D backward facing steps are approximately 19.4°, 7.5°, and 15.6°. Since the 6 mm rod does not have a defined shear layer, a shear layer growth rate an angle was not determined. These results indicate that the spread angle is a measure of larger vortices and as a consequence peak acoustic frequency decreases. Even though the flat spoiler's shear layer growth angle is significantly smaller, large scale vortices are produced that are slightly smaller than the baseline's vortex size. The growth angle for the large 3D backward facing steps is smaller but the device produces streamwise vortices that inhibit the large scale two dimensional vortices that the baseline, ridges and flat spoiler produce.

Figure 25 shows the DFT results for three flow control devices at the peak acoustic frequency. The peak acoustic frequency determined from power spectra refer to the frequency associated with

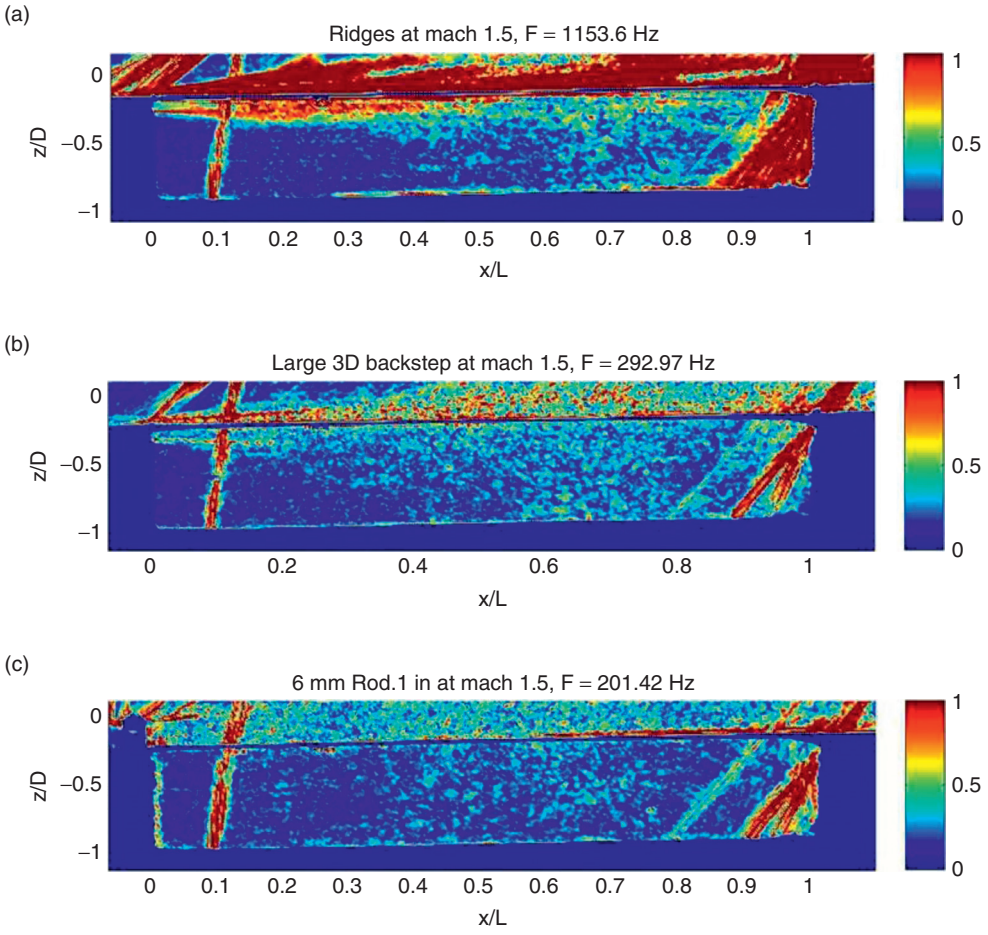


Figure 25. DFT of the shadowgraph images at maximum frequency, side view; (a) Ridges at F = 1153.6 Hz, (b) Large 3D Backward Facing Steps at 292.97 Hz. (c) 6 mm Rod at F = 201.4 Hz.

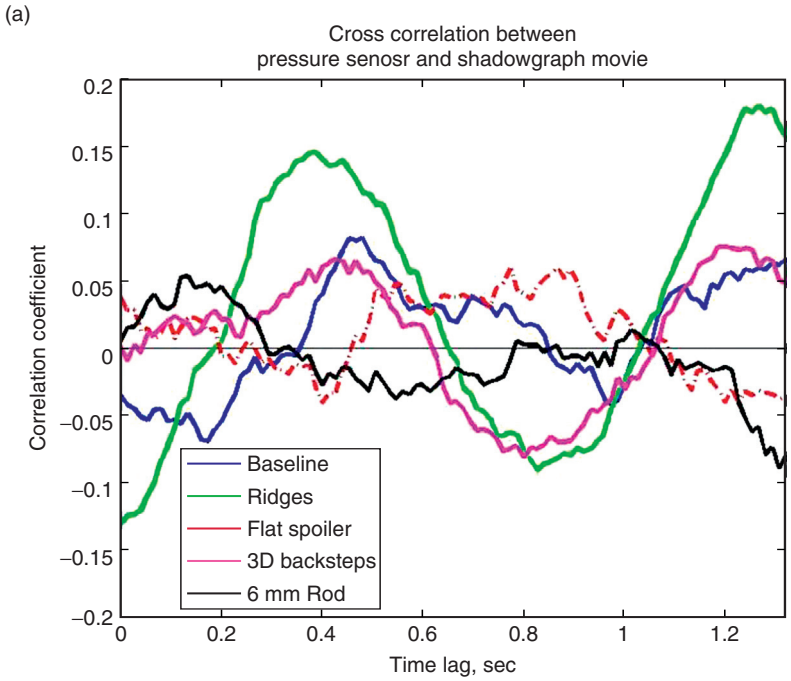


Figure 26. Cross correlation between the aft wall pressure sensor located at x/L = 1.00 and shadowgraph pixel intensity at x/L = 0.99, z/D = –0.50.

highest SPL. Results for the ridges device presented in Figure 25a show that at the peak acoustic frequency, the shear layer is the strongest feature of the flow and even slightly stronger than the baseline case. The side view results show that at this peak acoustic frequency the shear layer is the strongest feature in the flow field, and may be stronger than the baseline case. The new feature that is very noticeable below the waterline of the cavity extending downstream to x/L = 0.5 is the streamwise vortices that the ridges produce. Figure 25b shows the results for the large 3D backward facing steps at 292 Hz. Again the streamwise vortices that the large 3D backward facing steps produces are observable near the leading edge of the cavity below the waterline and extend downstream to approximately x/L = 0.2. Figure 25c shows the results for the 6 mm rod at 201 Hz. The flow features that are noticeable with this device are the shedding above and below the rod in the streamwise direction that extends downstream to about x/L = 0.1. All three of these devices have features that are highlighted at their respective frequency but this does not suggest that these flow features are being produced at their respective frequencies, but the density fluctuations that are being measured are at these frequencies.

Since the high speed shadowgraph movies were simultaneously sampled with the pressure sensors the pressure data was cross-correlated with the pixel intensity to determine correspondence between the two. Figure 26 shows the cross correlation between the pressure sensor located at x/L = 1.00 and the pixel intensity located at x/L = 0.99, z/D = –0.50. As previously shown in Figure 23 the cross correlation for the pixel intensity is relatively small and in turn the cross correlation between the pressure sensors and the pixel intensity is even smaller. Noting that the shadowgraph is an integrated optical path measurement and the pressure sensor is a single point measurement only a small portion along that path a correlation can be obtained and is likely to be weak since there are several different flow features interacting in that region. The ridges device followed by the baseline case has the largest correlation while the other flow control devices are relatively weaker, but are not zero indicating that there is a correlation between the shadowgraph measurements and the pressure sensors. The large correlation for the ridges device is a result of the very periodic shedding that this device creates.

### 3.4. Qualitative Results of Top View Results

High speed shadowgraph images viewed from the top of the cavity are discussed in this section. The three pixel locations examined are at x/L = 0.50, y/W = 0.00; x/L = 0.99, y/W = 0.00; x/L = 0.99, y/W = –0.25, for all flow control device tested, unless otherwise stated. The first two locations represent

two point in the along the centerline of the cavity at middle of the cavity and just upstream of the aft wall. The third location represents a point just upstream of the aft wall pressure sensor.

Figure 27 shows the time history of the pixel intensity for the three pixel locations stated above and for each of the geometry modifications devices tested. A value of 0 indicates a color of black in the movies while a value of 256 indicates a color of white, for most of the shadowgraph movies the pixel intensity is on the darker side because the contrast and brightness were adjusted to provide optimal discernible for the human eye. Figure 27a, b and c. are the pixel intensity time traces for baseline case at the three observed pixel locations, respectively. Figure 27d, e, and f are the pixel intensity time traces for the ridges case at the three observed pixel locations, respectively. Figure 27g, h, and i are the pixel intensity time traces for the flat spoiler case at the three observed pixel locations, respectively. Figure 27j, k, and l are the pixel intensity time traces for the large 3D backward facing steps case at the three observed pixel locations, respectively. Figure 27m, n, and o are the pixel intensity time traces for the 6 mm rod case at the three observed pixel locations, respectively.

It is evident from Figure 27 that the middle of the cavity is relatively quiet for all cases tested and is not surprising as the density fluctuations across the thickness of the shear layer are negligible compared to the streamwise gradients. As for the middle column of Figure 27b, e and h shows some spikes are present in baseline, ridges, and flat spoiler, respectively. These spikes are shear layer

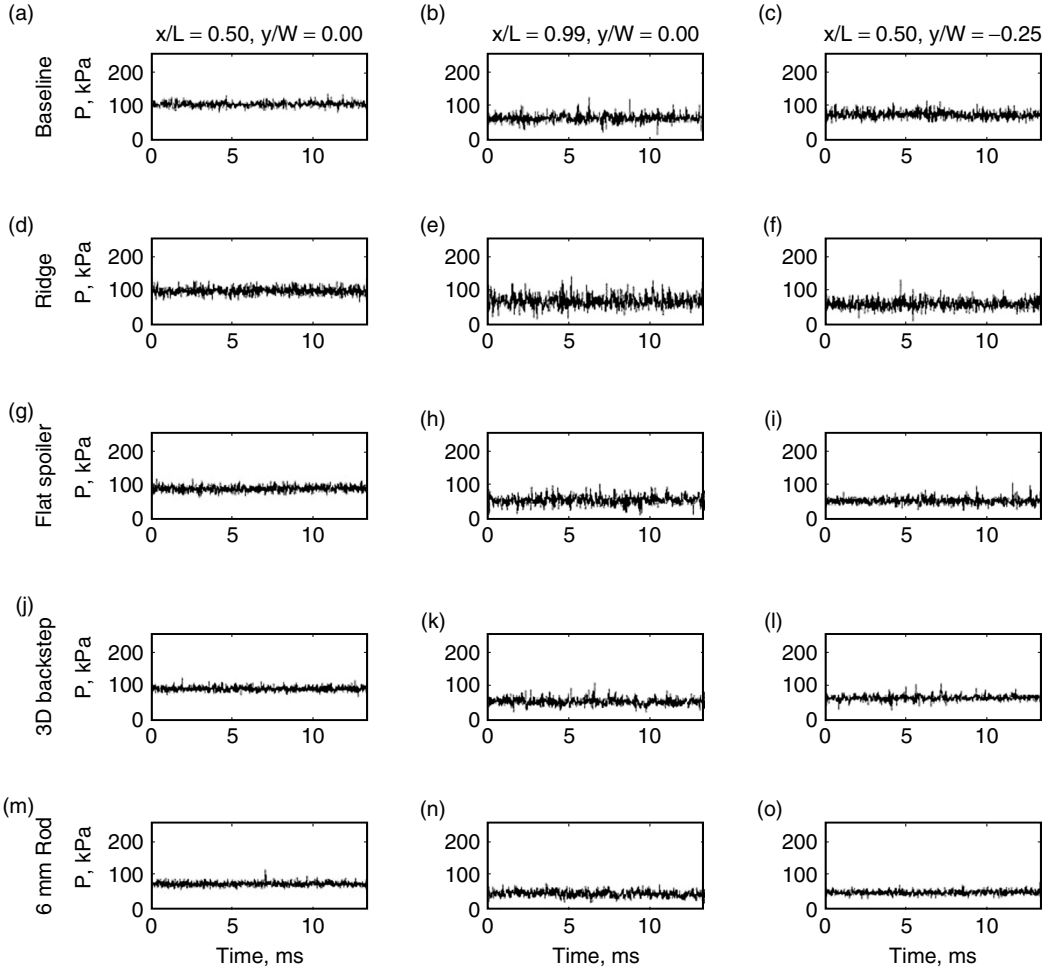


Figure 27. Time history of shadowgraph pixel intensity, top view. Left column: Sensor location x/L = 0.50 and y/W = 0.00, Middle column: Sensor location x/L = 0.99 and y/W 0.00, Right column: Sensor location x/L= 0.99 and y/W = –0.25. First Row: Baseline, Second Row: Ridges, Third Row: Flat Spoiler, Fourth Column: 3D Large Backward facing steps, Fifth Row: 6 mm Rod.

impingement on the rear wall that result in high density fluctuations The right column of Figure 27 show that the density fluctuations at an off-center location near the aft wall are not as strong as the centerline of the cavity and it is due to the bifurcated recirculation region depicted in Figure 9.

Results of 6 mm rod shown in the last row of Figure 27 indicate weakest pixel intensity even though the shear layer is thicker than the other cases. This is due to large scale mixing in the wake of the rod that in turn keeps the density fluctuations to a minimum [34].

Figure 28 shows the PDF's of the pixel intensity from the previous time traces for all three locations and geometry modifying flow control devices, for only 4096 images. Because of the limited number of samples and even lower quantization levels, as compared to the side view of the grey scale image, the pixel intensity's PDF profiles are not as smooth as the side view's PDF profiles, but they can again provide a general trend to gauge the usefulness of the high speed shadowgraph movies for this viewing direction. Figure 28a shows the PDF for the pixel location x/L = 0.50, y/W = 0.00 and shows that the profiles look Gaussian even though the number of quantization levels is low, e.g. 25 levels were used for Figure 28 whereas 100 and 35 were used for Figure 12 and 19 respectively. Figure 28b shows the PDF profiles for the pixel location x/L = 0.99, y/W = 0.00. The 6 mm rod and flat spoiler have an issue with the quantization levels around $\sigma = 1$ which indicates that the quantization levels need to be reduced further to properly get a better Gaussian like profile. Figure 28c is the PDF for the pixel location x/L = 0.99, z/D = –0.25. Again the 6 mm rod has significant quantization level issues but because the signal is very weak, a proper Gaussian profile may not be possible using the shadowgraph technique because the density fluctuations are weak.

Figure 29a shows the skewness for five streamwise locations along the centerline of the cavity. The horizontal line at 0.4 skewness is for reference purpose. For most of the flow control devices the

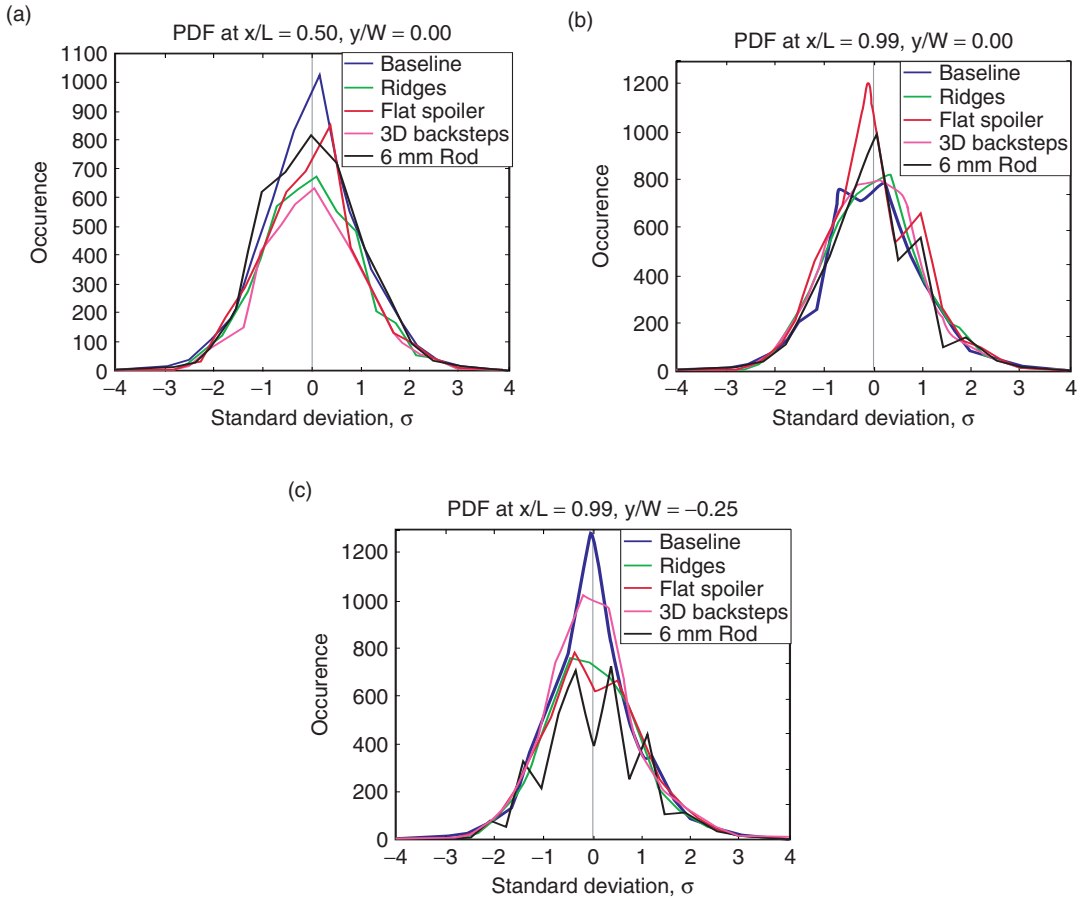


Figure 28. Probability Density Functions (PDF's) of the Shadowgraph pixel intensity, top view; (a) x/L = 0.50, y/W = 0.00, (b) x/L = 0.99, y/W = 0.00 and (c) x/L = 0.99, y/W –0.25.

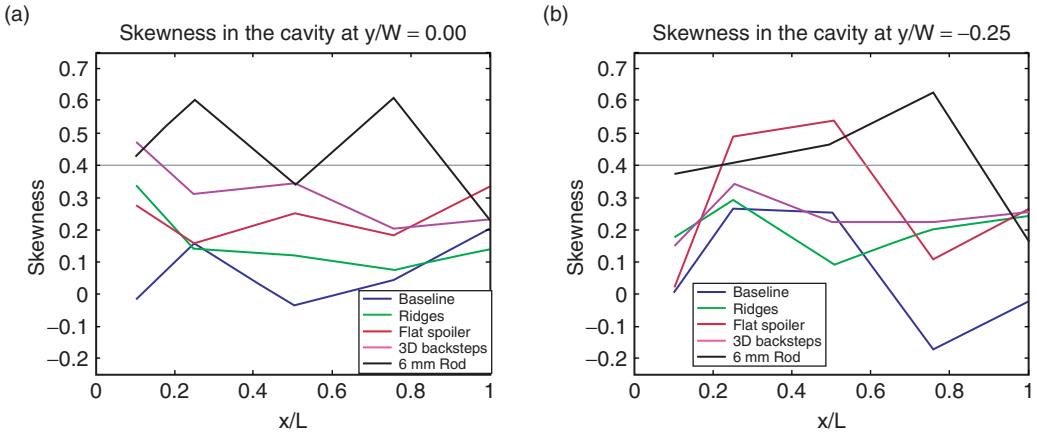


Figure 29. Skewness of the shadowgraph pixel intensity, top view; (a) y/W = 0.00, (b) y/W = –0.25.

skewness is below the 0.4 line indicating that the data is evenly distributed across the limited number of quantization levels. The 6 mm rod does have some high levels of skewness at x/L = 0.25 and 0.75 which may due to low quantization levels. Figure 29b shows the skewness for five x locations along the y/W = –0.25 axis. Again most of the cases have low levels of skewness except for the flat spoiler and the 6 mm rod, however these two flow control devices have small changes in the pixel intensity which biases the results.

In addition to the skewness it is important to examine the kurtosis. Figure 30a shows the kurtosis of the shear layer at five x locations y/W = 0.00. Figure 30b shows the kurtosis inside the cavity at five x locations at y/W = –0.25. Both figures indicate that the baseline and exhibit Guassian profile while the flow control devices are near Guassian. The 6 mm rod and the large 3D backward facing steps are non-Guassian due to the low quantization levels.

Figure 31a shows the autocorrelation for the intensity of the pixel location at x/L = 0.50, y/W = 0.00. For all but the flat spoiler, the autocorrelation coefficient quickly drops to less than a value of 0.1, which indicates that structures in the shear layer are not well defined along the span of the cavity. In the case of the flat spoiler, when examining the movie at this location, coherent streamwise structures are observed but there origin could not be determined. Figure 31b shows the autocorrelation for the pixel location x/L = 0.99, y/W = 0.00. The baseline and ridges time lag for the zero crossing is around t = 0.05 ms while the other flow control devices are significantly longer - approximately 0.2 ms for the flat spoiler and the larger 3D backward facing steps and 0.4 for the 6 mm rod. All cases do not decay to zero which shows that the repetitive nature of the flow field persists in this direction. Figure 31c shows the autocorrelation for the pixel location x/L = 0.99, y/W = –0.25 and for all the cases shown the time

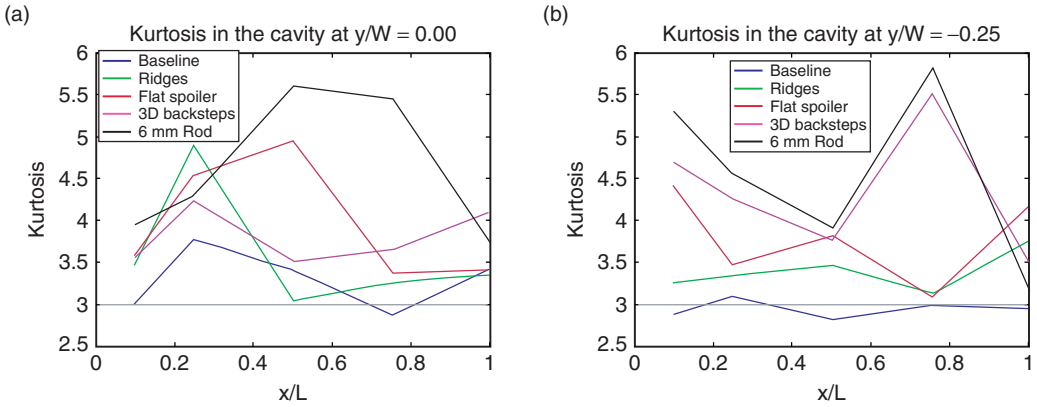


Figure 30. Kurtosis of the shadowgraph pixel intensity, top view; (a) y/W = 0.00, (b) y/W = –0.25.

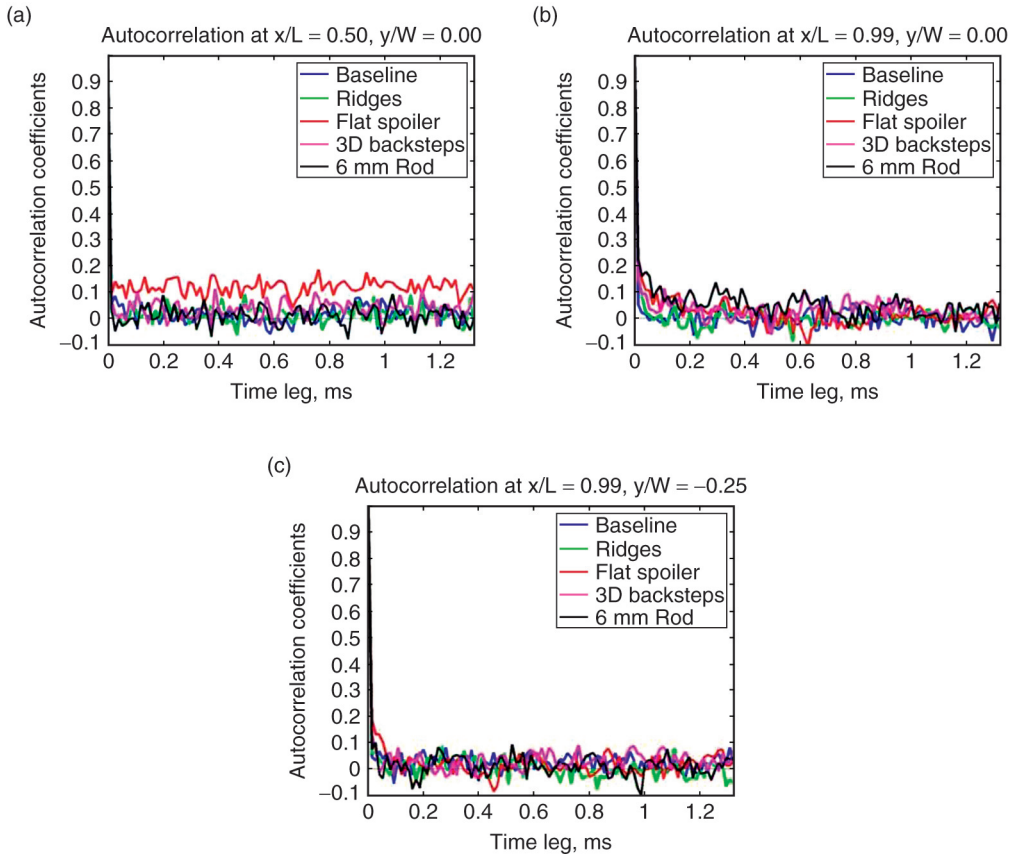


Figure 31. Autocorrelation of the shadowgraph pixel intensity top view; (a) x/L = 0.50, y/W = 0.00, (b) x/L = 0.99, y/W = 0.00 and (c) x/L = 0.99, y/W = –0.25.

lag is shorter than at the centerline which is due to the fact that it is being sampled in the bifurcated recirculation region.

Figure 32a shows the cross correlation between the pixel locations x/L = 0.50, y/W = 0.00 and x/L = 0.99, y/W = 0.00. As expected there is s slight correlation between the two points along the centerline of the cavity. For all the flow control cases the level of correlation is of the same order of magnitude as the baseline, showing indicating that flow control devices do not significantly change the shear layer development along the centerline of the cavity. Figure 32b shows the cross correlation between the pixel locations x/L = 0.50, y/W = 0.00 and x/L = 0.99, y/W = –0.25. The cross talk between the middle of the shear layer and the off center portion of the aft wall is negligible, which is expected since the aft wall location is in the middle of one of the bifurcated recirculation regions. Figure 32c shows the cross correlation between the pixel locations x/L = 0.99, y/W = 0.00 and x/L = 0.99, y/W = –0.25. The baseline and ridges case have the highest correlation at the aft wall of the cavity, which is expected since these cases produce a more coherent 2D shear layer across the cavity. With the other three flow control devices the shear layer starts to be less coherent and the cross correlation is decreases.

Figure 33 is the baseline case at 1190 Hz and it clearly shows that some of the strongest density fluctuations at peak acoustic frequency are along the sidewalls of the cavity including the aft wall. This suggests that the high density flow is travelling forward along the sidewalls. Figure 33b shows the results for the ridges device at 1190 Hz. Similar to the baseline case, ridges also exhibit strongest density fluctuations along the center of the aft wall of the cavity. The density fluctuations in this region are due to the vortices that become part of the bifurcated flow. Figure 33c shows the results for the flat spoiler at 1190 Hz. As with the baseline, Figure 33c similarly shows that the strongest density fluctuations are along the aft wall of the cavity but are not as strong. Again the aft wall density fluctuation is from the vortices traveling down the aft wall of the cavity due to the aft

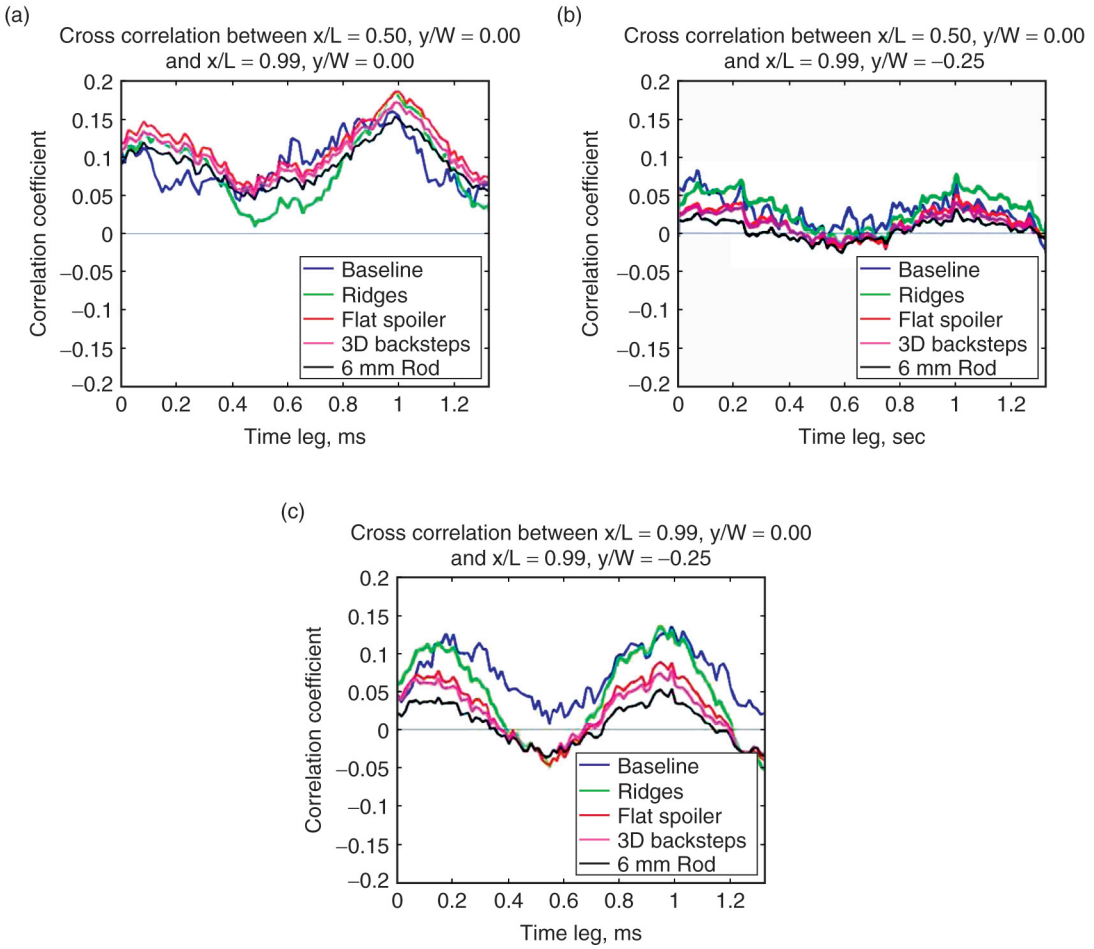


Figure 32. Cross correlation shadowgraph pixel intensity, top view; (a) Correlation between x/L = 0.50, y/W = 0.00 and x/L = 0.99, y/W = –0.25. (b) Correlation between x/L = 0.50, y/W = 0.00 and x/L = 0.99, y/W = 0.00, (c) Correlation between x/L = 0.99, y/W = 0.00 and x/L = 0.99, y/W = –0.25.

recirculation region. Figure 33d shows the results for the large 3D backward facing steps at 1190 Hz. The top view does not show strong density fluctuations. Figure 33e shows the results for the 6 mm rod at 1190 Hz. The side view shows that the shear layer does not dominate at the baseline's dominant frequency. The top view does not show density fluctuations that travel downstream towards the aft wall of the cavity.

The DFT results for three flow control devices are presented in Figure34. Figure 34a is the ridges device at 1153 Hz and streaks can be seen in the front of the cavity and are produced by the streamwise vortices that originate from the device. The frequency at which the streaks are produced may contribute to an increase in the peak acoustic tone. Figure 34b is the large 3D backward facing steps at 292 Hz. The visible streaks are a signature of the streamwise vortices that are produced. The larger spacing and streamwise vortex size provide longitudinal stability to the shear layer and keep the shear layer from producing large scale spanwise vortices that entrain freestream flow into the cavity. Figure 34c shows the 6 mm rod at 201 Hz. Two streaks are visible near the front of the cavity. These two streaks are the corner vortices at are produced by the posts that support the rod and may not contribute to the stability to the shear layer since most of the shedding from the rod reduces the formation of large shear layer vortices.

Figure 35 shows the cross correlation between the pressure sensor located at x/L = 1.00 and the intensity of the pixel located at x/L = 0.99, y/W = –0.25. As previously presented in Figure 32 the cross correlation for the pixel intensity is relatively small and in turn the cross-correlation between the

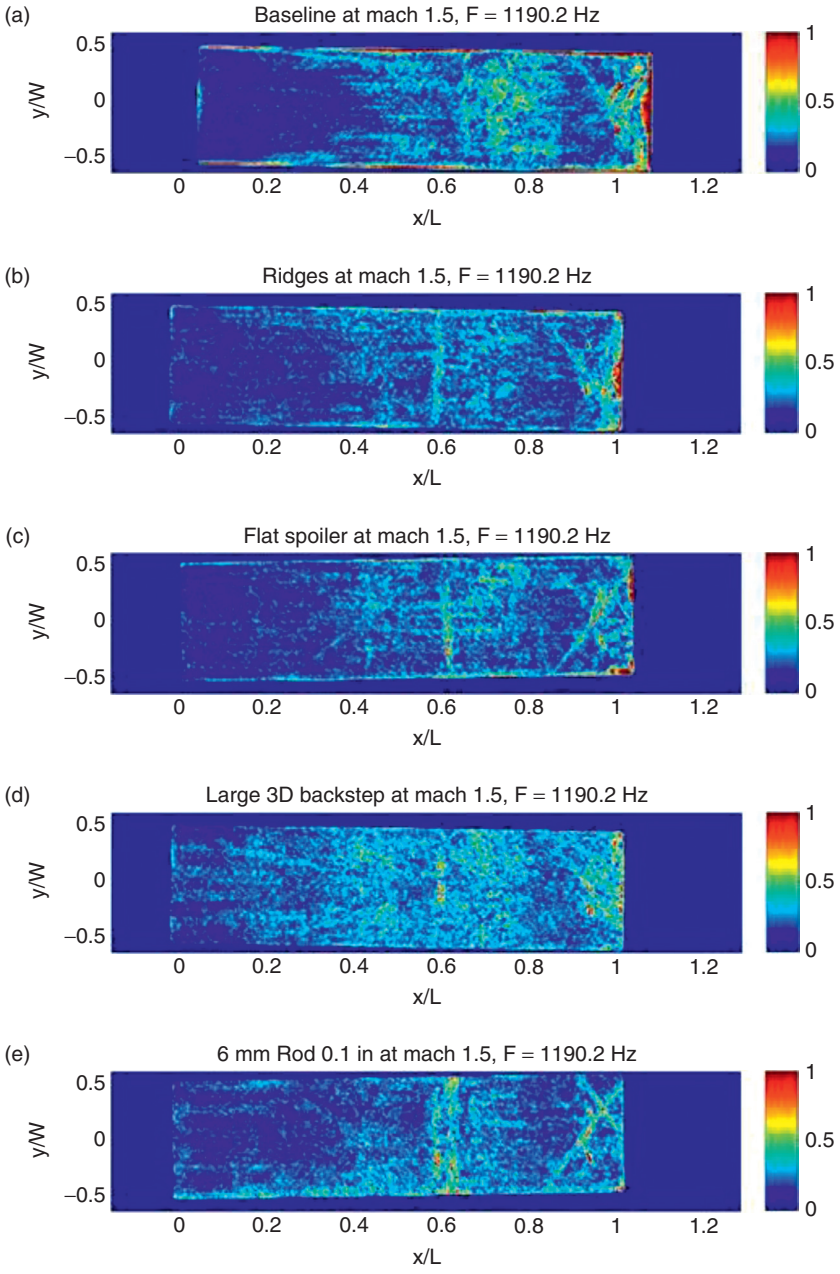


Figure 33. DFT of the shadowgraph images at F = 1190.2 Hz top view; (a) Baseline, (b) Ridges, (c) Flat Spoiler, (d) Large 3D Backward facing steps and (e) 6 mm Rod

pressure sensors and the pixel intensity is approximately the same. The ridges flow control device produces the best correlation values out of all the cases tested and is mainly due to the fact that the ridges case is very repeatable from the feedback mechanism that consistently produces large scale 2D vortices in the shear layer. The baseline has the next best correlation values and is due to the feedback mechanism producing the semi consistent large scale 2D vortices. The other three flow control devices have smaller correlation values suggesting that even very weak density fluctuations do correspond to measured pressure fluctuations.

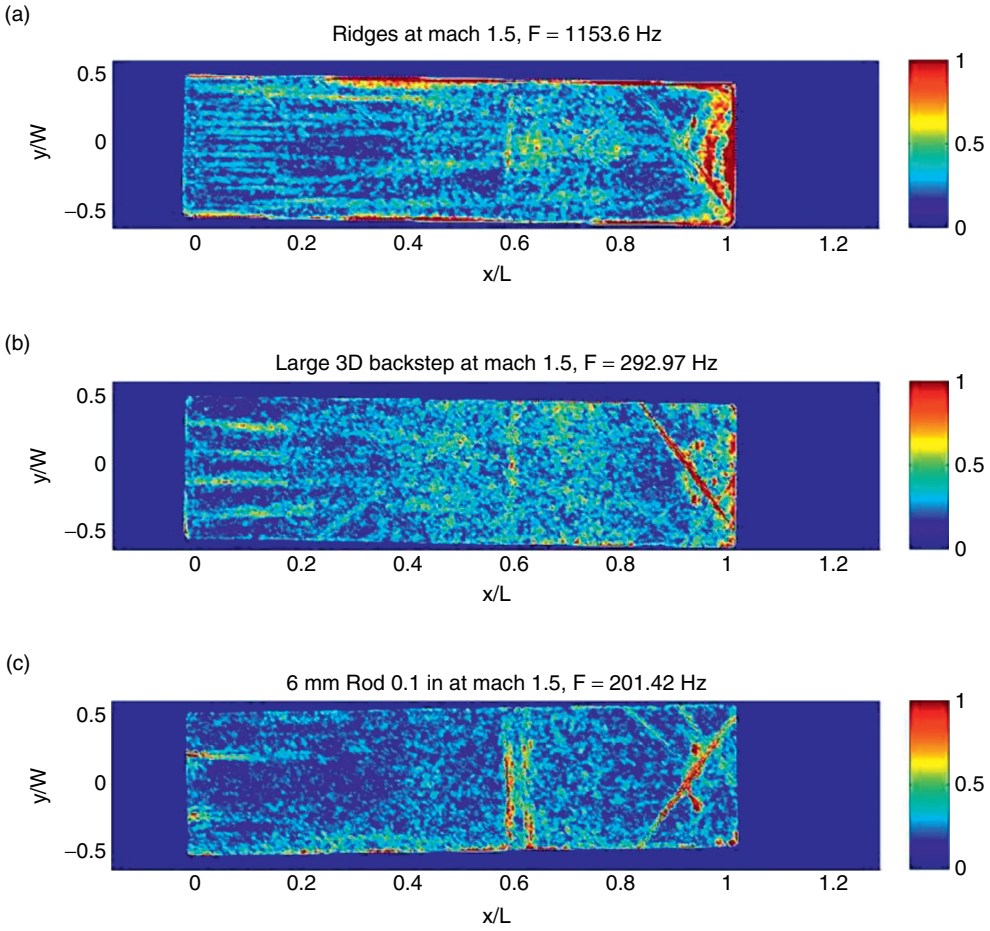


Figure 34. DFT of the shadowgraph images at maximum frequency top view; (a) Ridges at F = 1153.6 Hz, (b) Large 3D Backward Facing steps at 292.97 Hz. (c) 6 mm Rod at F = 201.4 Hz.

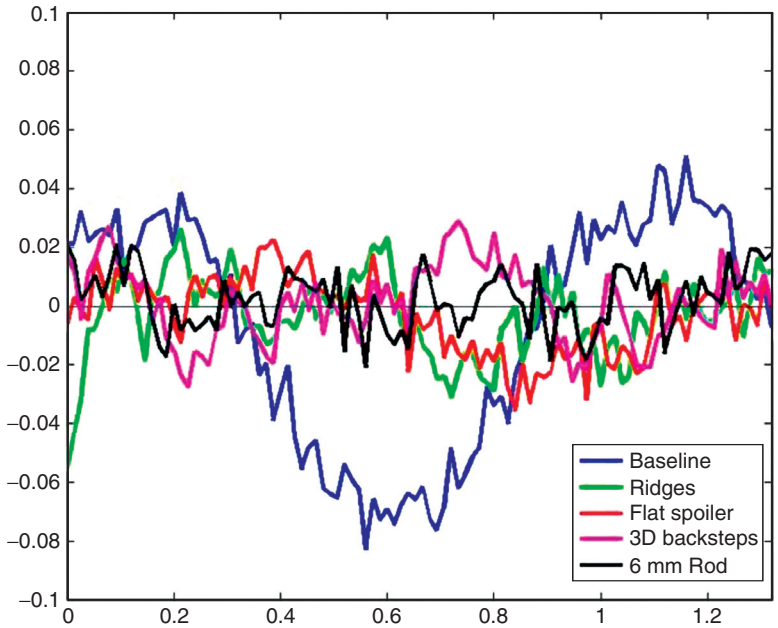


Figure 35. Cross correlation between the aft wall pressure sensor x/L = 1.00 and side view shadowgraph pixel intensity at x/L = 0.99, y/W = –0.25 for all geometry modification tested.

## 4. CONCLUSIONS

Developing an effective flow control device for supersonic conditions, to reduce or suppress the peak acoustic tone as well as the broadband noise, requires careful design. Stabilizing the shear layer with streamwise vortices is one method that shows promise, though the correct vortex spacing needs to be parametrically explored in detail. Vertical displacement of the shear layer is extremely hard at supersonic Mach numbers, so limiting the amount of fluid entrained into the cavity is probably a viable alternative. Even a small amount of fluid entrained into the cavity can initiate the acoustic cycle inside the cavity, as seen with the rod in cross flow results.

At Mach 1.5 the density fluctuations in the flow field are easily observable in the shadowgraphs. This allows for a very detailed comparison between the baseline and several passive flow control devices. Since the baseline cavity flow contains large vortical structures that traverse the cavity length with the shear layer, the reduction of broadband noise and acoustic tones pose a difficult challenge. However, passive flow modification devices do offer a viable solution to control the flow and reduce the broadband noise to an acceptable level.

Design of the flow control devices for applications in cavity flow is critical as evident from the results of ridges that introduced streamwise vortices superimposed on the shear layer however with intensified acoustic tones. On the other hand when streamwise vortices are introduced into the cavity, e.g. with large 3D backward facing steps with the correct spacing, they can be effective at reducing the acoustic tones by reducing the amount of flow entrained into the cavity. Even the rod in crossflow at supersonic conditions was not able to completely reduce the main acoustic tones. One possible reason is that the shedding from the rod results in more entrainment of the freestream flow towards the cavity and the radiation of waves at higher wave numbers acted as a resonator.

## REFERENCE

[1] K. Krishnamurty, *Acoustic Radiation from Two-Dimensional Rectangular Cutouts in Aerodynamic Surface*, 1955, NACA TN–3487.

[2] A. Roshko, *Some Measurements of Flow in a Rectangular Cutout*, 1955, NACA TN-3488.

[3] J.E. Rossiter, *Wind-Tunnel Experiments on the Flow over Rectangular Cavities at Subsonic and Transonic Speed*, 1966, Report and Memoranda No. 3438.

[4] H.H. Heller and D. Bliss, *The Physical Mechanism of Flow-Induced Pressure Fluctuations in Cavities and Concepts of their Suppression*, AIAA Paper, 1975, 491.

[5] C.K. Tam and P.J. Block, On the Tones and Pressure Oscillations induced by Flow Over Rectangular Cavities, *Journal of Fluid Mechanics*, 1978, 89, 373–399.

[6] R.C. Bauer and R.E. Dix, *Engineering Model of Unsteady Flow in a Cavity*, 1991, AEDC-TR-91-17

[7] L. Cattefesta, D. Williams, C. Rowley, and F. Alvi, *Review of active control flow induced cavity resonance*, AIAA Paper, 2003, 3567.

[8] L.N. Cattafesta, Q. Song, D. Willimas, C.W. Rowley, and F.S. Alvi, Active Control of Flow-Induced Cavity Oscillations, *Progress in Aerospace Sciences*, 2008, 44, 479–502.

[9] S.J. Moon, S.L. Gai, H.H. Kleine, and A.J. Neely, *Supersonic Flow Over Straight Shallow Cavities In Leading and Trailing Edge Modification* AIAA Paper, 2010, 4687.

[10] R.C. Murray and G.S. Elliott, Characteristics of the Compressible Shear Layer over a Cavity, *AIAA Journal,* 2001, 39, 846–856.

[11] J.G. Dudley and L. Ukeiley, *Suppression of Fluctuating Surface Pressure in a Supersonic Cavity Flow*, AIAA Paper, 2010, 4974.

[12] L.G. Kaufman and R.L. Clark, *Mach 0.6 to 3.0 Flows Over Rectangular Cavities*, 1983, AFWAL-TR-82-3112.

[13] M.J. Stanek, G. Raman, V. Kibens, J.A. Ross, J. Odedra and J.W. Peto (200) *Control of cavity resonance through very high frequency forcing*, AIAA Paper, 2000, 1905.

[14] R.F. Schmit and G, Ramen, High and low Frequency Actuation Comparison for a Weapons Bay Cavity, *International Journal of Aeroaoustics*, 2005, 5, 395.

[15] R.F. Schmit, C. McGaha, J. Tekell, J. Grove, and M. Stanek, (2009) *Performance Results for the Optical Turbulence Reduction Cavity*, AIAA Paper, 2009, 702.

[16] R.F. Schmit, F. Semmelmayer, M. Haverkamp, and J. Grove, *Fourier Analysis of High Speed Shadowgraph Images around a Mach 1.5 Cavity Flow Field,* AIAA Paper, 2011, 3961.

[17] G.F. Clark, *Trisonic Gasdynamic Facility User Manual*, 1982, AFWAL-TM-82-176-FIMM.

[18] J.P. Dussauge and A.J. Smits, Characteristic scales for energetic eddies in turbulent supersonic boundary layers, *Experimental Thermal and Fluid Sciences*, 1997, 14, 85–91.

[19] S.L. Birch, and J.M. Eggers, *A critical review of experimental data for developed free turbulent shear layers*, 1973, NASA SP321.

[20] C. Pantano, and S. Sarkar, A study of compressibility effects in the high-speed turbulent shear layer using direct simulation, *Journal of Fluid Mechanics*, 2002, 14, 329–371.

[21] N.T. Clemens and M.G. Mungal, Large-scale structures and entrainment in supersonic mixing layer, *Journal of Fluid Mechanics*, 1995, 248, 171–16.

[22] G.M. Lilley, The generation of sound in turbulent motion, *Aeronautical Journal*, 2008, 112, 381–394.

[23] W. Blumen, P.G. Dazing, D.F. Billings, Shear layer instability of inviscid compressible fluid, *Journal of Fluid Mechanics*, 1975, 71, 305–316.

[24] D. Papamoschou, and A. Roshko, The compressible turbulent shear layer: an experimental study, *Journal of Fluid Mechanics*., 1988, 197, 453–477.

[25] E. Schulein, and V.M. Trofimov, Steady longitudinal vortices in supersonic turbulent separated flows, *Journal of Fluid Mechanics*, 2011, 672, 451–476.

[26] M.J. Stanek, M.R.Visbal, D.P. Rizzetta, S.G. Rubin, and P.K. Khosla, On A Mechanism of Stabilizing Turbuelent Free Shear Layers in Cavity Flows, *Computers & Fluids*, 2007, 36, 1621–1637.

[27] X. Zhang, A. Rona, and J.A. Edwards, The effect of trailing edge geometry on cavity flow oscillations driven by a supersonic shear layer. *Aeronautical Journal*, 1998, 3, 129–136.

[28] G.L. Bar, *Experimental investigation of the sudden expansion of a supersonic plane flow into a 90oVee channel*, 1972, MS Thesis, Aerospace Engineering Department, Wichita State University, KS.

[29] A. Ahmed, and G.W. Zumwalt, Base Drag Reduction of a Non-Circular Missile, *Journal of Spacecraft and Rockets*, 1993, 30, 781–782.

[30] G.S. Settles, *Schlieren and Shadowgraph Techniques: Visualizing Phenomena in Transparent Media, 2006* Springer, Berlin.

[31] A.P.G. Peterson, E.E. Gross, *Handbook of Noise Measurements*. 1972, General Radio, Concord

[32] J.E.F Williams, J. Simpson, and V.J. Virchis 'Crackle': an annoying component of jet noise, *Journal of Fluid Mechanics*, 1975, 75.

[33] W.K. George, *Lectures in Turbulence for the 21st Century*, unpublished, 2011.

[34] M.J. Stanek, J.A. Ross, J. Odegra, J. Peto, *High Frequency Acoustic Suppression- The Mystery of the Rod-in-Crossflow Revealed*, AIAA Paper, 2003, 0007.